Mon. Not. R. Astron. Soc. **268,** 405–429 (1994)

Ginga observations of the X-ray spectra of Seyfert galaxies

K. Nandra[1,2] and K. A. Pounds[1]

[1] *X-ray Astronomy Group, Department of Physics and Astronomy, University of Leicester, University Road, Leicester LE1 7RH*
[2] *Institute of Astronomy, Madingley Road, Cambridge CB3 0HA*

Accepted 1993 December 21. Received 1993 November 25; in original form 1993 October 11

ABSTRACT

We present an analysis of 60 spectra of 27 Seyfert galaxies observed with the *Ginga* Large Area proportional Counter (LAC). The 2–10 keV continuum is found to be compatible with previous spectral surveys, but a spectral flattening, or 'hard tail', is evident above 10 keV. Excess absorption over the Galactic column density is found in around half of the sources, with an equivalent hydrogen column density $N_H = 10^{21-22}$ cm^{-2}. Spectral features are found to be common, with all but two of the sources showing evidence for an iron Kα emission line. The mean energy of the line, at around 6.4 keV, indicates an origin via fluorescence in near-neutral material. The mean equivalent width (100–150 eV) is large, considering that the sources are relatively unobscured. At least ~40 per cent of the sources show an additional improvement when an absorption edge is added, with an energy indicating an origin in highly ionized iron and equivalent hydrogen column density N_{HFe} of order 10^{23} cm^{-2}. These observations strongly imply the existence of two gas components – optically thick material and strongly photoionized gas of lower column density in the line of sight. The first is responsible for the bulk of the emission line, and Compton down-scattering and absorption result in a 'reflected' continuum component which produces the hard tail. The mean line and reflected continuum properties are in excellent agreement with those expected in a flattened geometry. Although other cold matter distributions are not ruled out, an origin in an accretion disc around the putative black hole seems most likely. The second component is highly ionized gas, the so-called 'warm absorber', which is responsible for the observed iron edge at 8–9 keV and complex absorption at soft X-ray energies. This plasma is difficult to detect at other wavelengths, and may form an outflow or wind. Both the reflection component and the warm absorber considerably modify the spectrum in the X-ray band, and previous observations with lower signal-to-noise ratio have resulted in misleading estimates of the spectrum of the underlying continuum. Rather than the $\Gamma = 1.7$ indicated by *HEAO-1* and *EXOSAT*, we find that the mean X-ray continuum is best modelled by a power law with photon index in the range $\Gamma = 1.9$–2.0. These observations have considerable implications for the power-production mechanism in active galactic nuclei (AGN), and provide important diagnostics of the accretion flow and environment around the central black hole.

Key words: galaxies: active – galaxies: Seyfert – X-rays: galaxies.

1 INTRODUCTION

The excess 'blue bump' emission observed in many AGN has long been interpreted as thermal emission from an accretion disc (Shields 1978; Malkan & Sargent 1982). An alternative to this popular interpretation was proposed by Guilbert & Rees (1988), who suggested that the blue bump might be generated via reprocessing of hard X-rays by optically thick 'cloudlets' close to the central source. Guilbert & Rees also predicted that these cloudlets would imprint features on the spectrum, which might be particularly visible in the X-ray region. It was quickly realized that *any* cold, optically thick

material, including an accretion disc, subtending a sufficiently large solid angle at the continuum source would leave imprints on the X-ray spectrum.

In order to test this hypothesis, Nandra et al. (1989) searched for the predicted spectral features, primarily an iron Kα emission line, in an extended *EXOSAT* medium-energy (ME) observation of the Seyfert 1 galaxy MCG-6-30-15. This feature, along with a corresponding absorption edge, was found, in extraordinary agreement with the prediction of Guilbert & Rees (1988). By this time, features were beginning to emerge in the first X-ray spectra obtained with *Ginga*. In particular, emission features were discovered in the spectra of three other Seyfert galaxies by Pounds et al. (1989), and confirmation of the emission line in MCG-6-30-15 was presented by Matsuoka et al. (1990) and Nandra, Pounds & Stewart (1990).

The most popular interpretation of the emission feature has been via fluorescence and reprocessing in an accretion disc, as opposed to the original cloud model of Guilbert & Rees (1988). Lightman & White (1988) showed that a broad hump of emission, peaking at 30–50 keV, would also be expected from an optically thick, reprocessing medium, such as an accretion disc, because of absorption and Compton down-scattering of the X-ray continuum photons. Fabian et al. (1989) presented calculations of the expected line profile from an accretion disc around a Schwarzschild black hole, and showed these to be a good fit to data obtained for Cyg X-1 with the *EXOSAT* gas-scintillation proportional counter (GSPC). This source shows a strong resemblance to AGN, and is suspected to represent a lower luminosity example of the same phenomenon. It is clear that the precise measurement of such iron *K*-shell features may yield valuable information on the geometry and physical state of the accretion flow in AGN.

Additional features arise from the so-called 'warm absorber', optically thin gas lying in the line of sight to the nucleus. The presence of such gas was first suggested by Halpern (1984) on the basis of a variable low-energy cut-off in the quasar MR 2251 − 178. Subsequently, similar flux-correlated variations in absorption have been suggested from *EXOSAT* and *Ginga* observations (e.g. Nandra et al. 1990; Pan, Stewart & Pounds 1990). The warm absorber provides a natural explanation for these variations. Any partially ionized gas in the line of sight, if of sufficient column density, will imprint absorption edges on to the X-ray spectrum. Where the elements responsible for the bulk of the opacity at ~ 1–2 keV (e.g., O, Ne, Mg, Si, Fe) are recombined, these absorption features produce an apparent cut-off in the low-energy spectrum. When the source brightens, these elements become more ionized, reducing the soft X-ray opacity. The most striking *individual* feature from the partially ionized absorber, in the *Ginga* band, is the iron edge, which occurs at 7.1 keV for neutral iron, increasing smoothly with ionization state to 9.29 keV for the hydrogen-like state. Good evidence for such an edge has been found in some individual *Ginga* observations (e.g., MCG-6-30-15, Nandra et al. 1990; NGC 5548, Nandra et al. 1991; NGC 7172, Warwick et al. 1993). Final, confirming evidence for the warm absorber hypothesis has come from recent *ROSAT* observations, which have shown evidence for an absorption feature arising from highly ionized oxygen (O VII–VIII) in the soft X-ray spectra of several AGN (Nandra & Pounds 1992; Fiore et al. 1993; Nandra et al. 1993; Turner et al. 1993), with an optical depth and energy consistent with the ionization state inferred from the *Ginga* measurements of the iron edge. The better definition of the column density and ionization parameter of the warm absorber derived from the *ROSAT* observations suggests that, in addition to the iron edge, there should be significant imprints on the *Ginga* spectra at soft X-ray energies. These should manifest themselves as a significant low-energy column, which may not be adequately described by the opacity profile for neutral material, such as that given by Morrison & McCammon (1983).

The emergence of several of the features described above stimulated an extensive programme of spectral monitoring of Seyferts using *Ginga*. Here we present a comprehensive analysis of 60 observations of 27 individual AGN. Results on smaller samples of AGN have already been presented by Pounds et al. (1990), Awaki (1991) and Nandra (1991). In the first half of this paper, we concentrate on a parametrization of the spectra, without reference to a specific physical model. Later, we discuss possible models for the observed features. The observations strongly indicate a preference for X-ray reflection from cold, optically thick material, to account for the iron line and the spectral flattening at high energies, together with absorption by partially ionized material in the line of sight. Our sample analysis has enabled us to show that these features are extremely common, if not ubiquitous, in the X-ray spectra of Seyfert galaxies, and allowed us to define mean parameters for the sample for comparison with theoretical models.

2 THE *GINGA* SAMPLE

The sample is listed in Table 1. The majority are bright (>1 mCrab), hard-X-ray-selected AGN, with luminosities L_x(2–10 keV) in the range 10^{41}–10^{45} erg s^{-1} (in this work $H_0 = 50$ km s^{-1} Mpc^{-1} and $q_0 = 0.5$ are assumed throughout). For a discussion of the X-ray spectral properties of higher luminosity emission-line AGN, the reader is referred to Williams et al. (1992). We have also excluded all classical Seyfert 2 galaxies from our sample (see Awaki 1991 for details of these), all AGN with known strong contaminating sources in the LAC field-of-view, and weak sources with 2–10 keV count rates below 3.5 count s^{-1} (approximately representing the 5σ detection level) to provide the best sample possible for spectral analysis.

3 PRELIMINARY ANALYSIS

All the data presented in this paper were obtained using the Large Area proportional Counter (LAC) aboard *Ginga* (Makino et al. 1987). The *Ginga* observation log for our sample sources is shown in Table 2. The LAC instrument covers a nominal energy range of 1.5–37 keV with energy resolution of $44E^{-0.5}$ per cent, where E is the energy measured in keV, and a total effective area of about 4000 cm^{-2} (see Turner et al. 1989 for a full description of the instrument).

All data were accumulated in the LAC MPC 1 data mode, with full 8-detector identification, 48-channel PHA resolution and separation of top and mid-layer spectra. The lower signal-to-noise ratio of the mid-layer data means that they do not provide additional spectral constraints for relatively

Table 1. The *Ginga* sample of Seyfert galaxies.

Name	Galaxy Type	R.A. (1950)	DEC (1950)	z	No. obs
Mrk 335	Sy 1	00 03 45	+19 55 29	0.026	4
NGC 526A	NELG	01 21 37	−35 19 32	0.018	1
Fairall-9	Sy 1	01 21 51	−59 03 58	0.046	1
3C 111	Sy 1	04 15 01	+37 54 20	0.048	1
Akn 120	Sy 1	05 13 38	−00 12 15	0.033	1
NGC 2110	NELG	05 49 47	−07 28 02	0.007	1
NGC 2992	NELG	09 43 18	−07 22 47	0.008	1
NGC 3227	Sy 1.5	10 20 47	+20 07 06	0.004	2
MCG-5-23-16	NELG	09 45 28	−30 42 57	0.008	2
NGC 3516	Sy 1	11 03 23	+72 50 25	0.009	3
NGC 3783	Sy 1	11 36 33	−37 27 41	0.01	1
NGC 4051	Sy 1	12 00 36	+44 48 35	0.002	3
NGC 4593	Sy 1	12 37 04	−05 04 01	0.009	2
MCG-6-30-15	Sy 1	13 33 02	−34 02 27	0.008	3
IC 4329A	Sy 1	13 46 28	−30 03 41	0.014	1
NGC 5506	NELG	14 10 39	−02 58 26	0.006	1
NGC 5548	Sy 1	14 15 43	+25 22 01	0.017	11
Mrk 841	Sy 1	15 01 36	−10 37 59	0.036	3
3C 382	Sy 1	18 33 12	+32 39 18	0.058	3
3C 390.3	Sy 1	18 45 38	+79 43 07	0.056	1
Mrk 509	Sy 1	20 41 26	−10 54 18	0.036	4
H2106-099	Sy 1.2	21 06 28	−09 52 30	0.027	2
NGC 7172	NELG	21 58 56	−32 07 54	0.008	1
NGC 7213	Sy 1	22 06 07	−47 24 39	0.006	2
NGC 7314	NELG	22 33 01	−26 18 17	0.006	1
NGC 7469	Sy 1	23 00 44	+08 36 25	0.017	1
MCG-2-58-22	Sy 1	23 02 08	−08 57 19	0.048	4

weak sources such as these, but they are valuable as a background-subtraction diagnostic (Hayashida et al. 1989). The spectra in the sample were analysed uniformly, with similar data-selection criteria applied to all observations according to the following prescription. First, a data cube (with full time and spectral information) was produced by sorting the first reduction files (FRFs). Periods of high background were removed by excluding regions of high SUD (counts, almost all background, above the upper discriminator, in this case 22 keV). Because of the decay of the *Ginga* orbit during 1990–91, and subsequent reduction in total background rates, this constraint was tightened for observations made towards the end of the mission (a range of $SUD_{max} = 7$–10 count s^{-1} detector^{-1} was used over the lifetime of the mission). Note that higher SUD limits are generally applied to background observations, to provide more data for the modelling. Areas of low geomagnetic rigidity (< 10 GeV/c) were also excluded, to avoid periods of high cosmic-ray-induced background, as were periods when the solid-state electron monitor (SOL) count rate exceeded 15 count s^{-1}.

We have also applied standard cleaning algorithms to the data, to remove periods when background-dominated or bad-quality data exist. This procedure involved two stages. First, the SUD count rate and Physical Instrument (PI) count rate were compared. Both of these are good measures of the particle background, and are highly correlated during periods when the background is well behaved. Points lying $> 3\sigma$ from this correlation were deleted. Next, the counts in adjacent spectral channels of the LAC were compared. Given the spectral resolution of the LAC instrument, a strong correlation is expected, and generally observed, between these. Dramatic background events and poor-quality data can be identified by this method, as these often produce discontinuities in pulse-height space. In our analysis, points lying $> 5\sigma$ from this correlation were removed from further analysis. Background-subtraction of the accepted data was then carried out according to the standard prescription of Hayashida et al. (1989). We have generally applied two separate background-subtraction methods. One method uses data adjacent in time to the source observations (if available), meaning that the effect of the 37-d background cycle associated with the spacecraft attitude at the time of passage through the South Atlantic Anomaly is negligible. The other method uses some (typically ~ 3) months of background data to simulate this cycle explicitly. Whilst a quantitative assessment of the quality of the background-subtraction is difficult, in general we have found that the second method of background subtraction gave better results.

After background-subtraction of the data cube, the time data were compressed to produce a one-dimensional spectrum to which systematic errors of 0.02 count s^{-1} per channel were added below 10 keV and 0.01 count s^{-1} per channel above 10 keV. We then employed a standard spectral-fitting technique, whereby various models were folded through the LAC response matrix and compared, using a χ^2 test, to the data, iterating until a minimum statistic was achieved. Confidence regions were calculated according to the prescription of Lampton, Margon & Bowyer (1976). We have used a conservative prescription, assuming all but one of the free parameters to be of interest in the error calculation and the 68 per cent confidence limit, which should in most cases provide a conservative estimate of the 1σ error on any given parameter. We have generally restricted our spectral fits to the 2–18 keV range, to avoid contamination by silver fluorescence from the collimator at ~ 22–25 keV. The data above this energy are of very low statistical weight, and add little to the constraints.

The ultimate sensitivity of the LAC is limited by spatial variations in the diffuse background contribution, which amount to ~ 0.7 count s^{-1} in the 2–10 keV band (1σ). Such fluctuations can add considerably to the uncertainty in the derived spectral parameters for very weak sources. However, our requirement of using only sources with count rates > 3.5 count s^{-1} means that, even for the weaker sources discussed here, these uncertainties contribute only a few per cent error to the derived photon index and can be ignored during the

Table 2. *Ginga* observation log.

Name	Start Date	Exp.[a] (ks)	Count[b] rate	F_x^c (2–10 keV)	L_x^d
Mrk 335 (1)	1987–Dec–03	17.6	4.1 ± 0.1	0.91 ± 0.16	2.7
Mrk 335 (2)	1988–Nov–25	22.6	9.5 ± 0.1	2.00 ± 0.16	6.0
Mrk 335 (3)	1990–Dec–22	25.5	5.2 ± 0.1	1.07 ± 0.15	3.1
Mrk 335 (4)	1991–Jul–02	19.9	5.8 ± 0.2	1.25 ± 0.15	3.7
NGC 526A	1988–Dec–15	18.7	4.4 ± 0.1	1.06 ± 0.17	1.5
Fairall 9	1990–Nov–22	36.9	14.2 ± 0.1	3.09 ± 0.18	29.0
3C 111	1989–Feb–04	18.9	13.6 ± 0.1	3.13 ± 0.19	32.0
Akn 120	1988–Sep–22	7.7	16.3 ± 0.2	3.58 ± 0.19	17.0.
NGC 2110	1989–Sep–26	19.2	14.1 ± 0.1	3.35 ± 0.19	0.71
NGC 2992	1990–Apr–30	32.9	7.2 ± 0.1	1.68 ± 0.17	0.46
MCG-5-23-16 (1)	1988–Nov–30	5.2	18.8 ± 0.1	4.39 ± 0.21	1.2
MCG-5-23-16 (2)	1988–Dec–05	5.0	9.2 ± 0.1	2.24 ± 0.18	0.6
NGC 3227 (1)	1988–Apr–16	31.8	18.0 ± 0.1	4.02 ± 0.20	0.28
NGC 3227 (2)	1990–Dec–09	22.8	17.3 ± 0.1	3.92 ± 0.20	0.27
NGC 3516 (1)	1989–Oct–07	39.2	9.8 ± 0.1	2.42 ± 0.19	0.85
NGC 3516 (2)	1989–Oct–12	13.4	8.1 ± 0.1	2.07 ± 0.19	0.72
NGC 3516 (3)	1989–Oct–19	6.8	8.3 ± 0.1	2.09 ± 0.19	0.73
NGC 3783	1990–Jan–13	17.5	24.7 ± 0.1	5.77 ± 0.24	2.5
NGC 4051 (1)	1987–Jun–03	30.5	7.4 ± 0.1	1.67 ± 0.17	0.03
NGC 4051 (2)	1988–May–13	39.3	8.6 ± 0.1	1.92 ± 0.17	0.03
NGC 4051 (3)	1990–Nov–21	6.0	8.8 ± 0.1	1.95 ± 0.17	0.03
NGC 4593 (1)	1987–Jun–25	14.0	11.8 ± 0.1	2.68 ± 0.18	0.94
NGC 4593 (2)	1987–Dec–13	7.4	16.1 ± 0.1	3.58 ± 0.19	1.2
MCG-6-30-15 (1)	1987–Sep–08	21.3	13.1 ± 0.1	3.63 ± 0.22	1.0
MCG-6-30-15 (2)	1989–Jun–24	19.1	25.6 ± 0.1	5.59 ± 0.23	1.5
MCG-6-30-15 (3)	1990–Feb–01	52.6	33.3 ± 0.1	7.28 ± 0.27	2.0
IC 4329A	1989–Jul–08		55.9 ± 0.1	12.30 ± 0.40	15.0
NGC 5506	1988–Jul–19	20.6	33.3 ± 0.1	7.87 ± 0.29	1.2
NGC 5548 (1)	1988–Jun–25	20.0	18.3 ± 0.1	4.08 ± 0.20	5.1
NGC 5548 (2)	1989–Jan–09	4.7	12.1 ± 0.1	2.88 ± 0.19	3.6
NGC 5548 (3)	1989–Jan–28	36.9	21.6 ± 0.1	4.98 ± 0.22	6.2
NGC 5548 (4)	1989–Jun–08	11.3	16.7 ± 0.1	3.79 ± 0.20	4.7
NGC 5548 (5)	1989–Jul–13	21.6	23.4 ± 0.1	5.22 ± 0.22	6.5
NGC 5548 (6)	1990–May–24	46.6	18.8 ± 0.1	4.20 ± 0.20	5.3
NGC 5548 (7)	1990–Jun–05	14.5	10.5 ± 0.1	3.19 ± 0.23	4.0
NGC 5548 (8)	1990–Jun–12	14.0	22.7 ± 0.1	5.08 ± 0.22	6.3
NGC 5548 (9)	1990–Jun–26	12.9	10.9 ± 0.1	2.48 ± 0.18	3.1
NGC 5548 (10)	1990–Jul–02	22.4	9.4 ± 0.1	2.12 ± 0.17	2.6
NGC 5548 (11)	1990–Jul–08	8.1	10.9 ± 0.1	2.43 ± 0.17	3.0
Mrk 841 (1)	1990–Jul–23	19.4	4.1 ± 0.1	0.92 ± 0.16	5.1
Mrk 841 (2)	1991–Jan–24	4.4	3.6 ± 0.1	0.79 ± 0.16	4.5
3C 382 (1)	1989–Jul–20	15.6	5.7 ± 0.1	1.30 ± 0.17	19.0
3C 382 (2)	1989–Jul–21	17.6	5.5 ± 0.1	1.24 ± 0.16	18.0
3C 382 (3)	1989–Jul–22	28.4	5.5 ± 0.1	1.27 ± 0.17	19.0
3C 390.3	1988–Nov–11	38.3	21.2 ± 0.1	4.67 ± 0.21	65.0
Mrk 509 (1)	1988–Oct–08	12.1	26.1 ± 0.1	5.70 ± 0.23	32.0
Mrk 509 (2)	1988–Oct–11	10.6	22.5 ± 0.1	5.00 ± 0.22	28.0
Mrk 509 (3)	1989–Oct–18	27.5	19.7 ± 0.1	4.35 ± 0.20	25.0
Mrk 509 (4)	1990–Oct–24	17.5	16.6 ± 0.1	4.96 ± 0.26	28.0
H 2106-099 (1)	1988–May–17	22.5	6.1 ± 0.1	1.32 ± 0.16	4.2
H 2106-099 (2)	1988–May–22	13.1	5.1 ± 0.1	1.12 ± 0.16	3.6
NGC 7172	1989–Oct–26	18.2	15.9 ± 0.1	4.13 ± 0.22	1.1
NGC 7213 (1)	1990–Jun–23	19.1	15.8 ± 0.1	3.53 ± 0.19	0.55
NGC 7213 (2)	1990–Oct–29	21.4	14.3 ± 0.1	4.24 ± 0.24	0.66
NGC 7314	1988–Oct–27	16.1	12.6 ± 0.1	2.83 ± 0.18	0.44
NGC 7469	1988–Jul–09	24.8	16.9 ± 0.1	3.69 ± 0.19	4.6
MCG-2-58-22 (1)	1989–Jun–19	15.0	8.1 ± 0.1	1.85 ± 0.17	19.0
MCG-2-58-22 (2)	1989–Jul–05	11.0	9.9 ± 0.1	2.27 ± 0.18	23.0
MCG-2-58-22 (3)	1989–Nov–05	15.2	7.6 ± 0.1	1.76 ± 0.17	18.0
MCG-2-58-22 (4)	1989–Nov–24	22.0	12.0 ± 0.1	2.78 ± 0.18	28.0

[a]Approximate exposure time. [b]count s^{-1} in the top layer only, 2–10 keV band. [c]Flux in units of 10^{-11} erg cm^{-2} s^{-1}. [d]2–10 keV luminosity in units of 10^{43} erg s^{-1}.

spectral analysis. This is partly because the spectrum of the fluctuations is rather similar to that of these AGN. We have, however, accounted for these in our determination of the flux error in Table 2, which also includes the statistical (Poisson) errors and an additional 3 per cent systematic error to account for uncertainties in the attitude solution and correction.

3.1 Trial models

Initially, the *Ginga* spectra were tested against several simple trial models, as follows, where $F_x(E)$ is the flux at energy E, A is the normalization, equivalent to the flux at 1 keV, and E is the energy in keV.

(1) Power-law:

$$F_x(E) = AE^{-\Gamma}\exp(-\sigma_{ph}N_H) \quad \text{photon cm}^{-2}\,\text{s}^{-1}\,\text{keV}^{-1}, \quad (1)$$

where Γ is the photon index, σ_{ph} is the photoelectric absorption cross-section (here the cosmic abundances and cross-sections of Morrison & McCammon 1983 are adopted), and N_H is the equivalent hydrogen column density of the absorbing material.

(2) Power-law plus Gaussian emission line:

$$F_x(E) = \left\{AE^{-\Gamma} + \frac{I_{K\alpha}}{\sqrt{(2\pi)}\,\sigma_{K\alpha}}\exp[-(E-E_{K\alpha})^2/2\sigma_{K\alpha}^2]\right\} \times \exp(-\sigma_{ph}N_H) \quad \text{photon cm}^{-2}\,\text{s}^{-1}\,\text{keV}^{-1}, \quad (2)$$

where $I_{K\alpha}$ is the integrated line flux in photon cm^{-2} s^{-1}, $\sigma_{K\alpha}$ the 1σ width of the Gaussian, and $E_{K\alpha}$ the centroid energy of the line, in keV. The equivalent width of the line is defined as

$$W_{K\alpha} = \frac{I_{K\alpha}}{F_c(E_{K\alpha})}, \quad (3)$$

where F_c is the continuum flux.

(3) Power-law plus iron absorption edge:

$$F_x(E) = AE^{-\Gamma}\exp(-\sigma_{ph}N_H) \times \exp(-\sigma_{Fe}N_{HFe}) \quad \text{photon cm}^{-2}\,\text{s}^{-1}\,\text{keV}^{-1}, \quad (4)$$

where σ_{Fe} is the iron K-absorption cross-section, given by

$$\sigma_{Fe} = \begin{cases} 0 & \text{if } E < E_{th} \\ \sigma_{th}E^{-\delta} & \text{otherwise.} \end{cases}$$

σ_{th} is the absorption cross-section at the threshold energy, E_{th}. These are both functions of ionization state. The index δ is only a slowly varying function of ionization. For neutral iron $\delta \sim 3.1$. N_{HFe} is the equivalent hydrogen column density corresponding to a solar abundance of iron. N_{HFe} is equal to the product of N_H and the iron abundance.

These last two models were also fitted in combination.

4 SPECTRAL INDEX

4.1 2–18 keV index

Initially, simple power-law plus absorption fits (equation 1) were tried in the 2–18 keV range. Statistically, the counts in the 2–10 keV range dominate these fits, given the reducing sensitivity of the LAC detector as a function of energy, and decreasing photon flux to higher energies. The fits are there-

fore affected little by including the counts above 10 keV, and are very similar to those in the 2–10 keV range. Such fits were generally very poor, with an excess at ~6.5 keV dominating the residuals, as for the individual sources described in the introduction. To illustrate the general trend of the residuals, we show, in Fig. 1(a), the residuals from a simple power-law fit to a data set produced by adding all 60 Seyfert spectra together, similar to the technique of Pounds et al. (1990). It is a very poor fit, with the iron line clearly visible. In fact, 36 of the 60 individual fits have $\chi^2_\nu > 1.4$, unacceptable at the ~90 per cent confidence level. Many fits are considerably worse than this (see Table 3 for details of the individual power-law fits; column 5 shows the reduced χ^2). However, this model was retained as a simple parametrization of the spectrum in order to allow comparison with previous spectral surveys and to test the validity of the 'canonical' photon index over the full 2–18 keV energy range.

Column 3 of Table 3 details the spectral indices, together with N_H (column 4) for these fits. A histogram of the spectral indices, obtained with these simple power-law plus absorption fits in the 2–18 keV range, of the *Ginga* sample is shown in Fig. 2. Where multiple observations exist, a weighted mean value has been taken, with the weight being taken as the mean of the two-sided errors. We recognize that this is not formally correct, but given our conservative error prescription we are confident that this will not lead to spurious conclusions, and we have used this technique in determining all future mean values. The most common value for Γ lies in the bin $\Gamma_{2\text{-}18} = 1.7\text{–}1.8$, with a weighted mean index $\overline{\Gamma}_{2\text{-}18} = 1.761 \pm 0.003$, consistent with both the *HEAO-1* (Mushotzky 1984) and *EXOSAT* (Turner & Pounds 1989) ME (2–10 keV) spectral surveys. To test for any intrinsic dispersion in the spectral index, compared to that expected from the measurement errors, the method of Maccacaro et al. (1988) has been followed. Using a maximum-likelihood technique, this allows confidence limits to be placed on the mean and standard deviation of the parent population, given a set of measurements and their errors.

The likelihood function to be maximized is

$$\mathscr{L} = \prod_{n=1}^{N} 1/\sqrt{2\pi(\sigma_p^2 + \sigma_n^2)}\, \exp[-(a_n - \langle\mu_p\rangle)^2/2(\sigma_p^2 + \sigma_n^2)], \qquad (5)$$

where μ_p and σ_p are the expectation values of the mean and intrinsic deviation of the parent population, and a_n are the measurements with associated errors σ_n. The best fit can be estimated by minimizing the statistic $S = -2 \log \mathscr{L}$, and confidence limits calculated using a deviate identical to that used when calculating limits for the χ^2 statistic (e.g. Lampton, Margon & Bowyer 1976). Using this method, an estimate for the mean spectral index $\langle\Gamma_{2\text{-}18}\rangle = 1.73 \pm 0.05$ ($\equiv \mu_p$) is found,

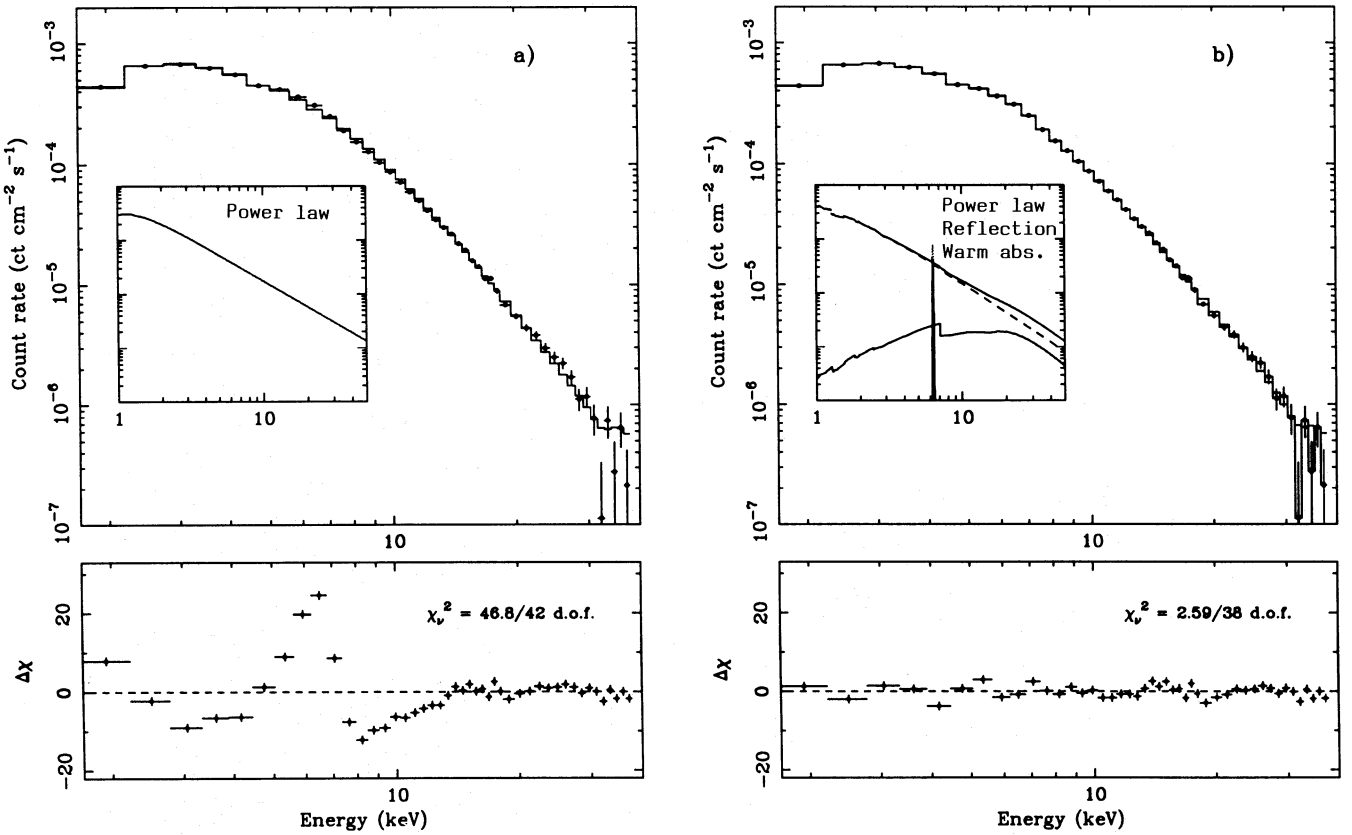

Figure 1. Input model (insets), count spectrum (top panels) and residuals (lower panels) to (a) a simple power-law fit to the summed data for all 60 observations of the 27 Seyferts in this sample. There are clear deviations, particularly in the region where the iron features are expected. The goodness-of-fit, as measured by the reduced χ^2 for the power-law fit, shows that this model is unacceptable, for both this summed data set and the bulk of the individual observations shown in Table 3. (b) A fit to the more complex model, which includes a reflection continuum, iron line and ionized absorber (see text). It is clearly a far better fit.

1994MNRAS.268..405N

Table 3. Power-law fits.

Name	A[a]	Γ_{2-18}	N_H[b]	χ^2_ν[c]	Γ_{10-18}	χ^2_ν[d]
Mrk 335 (1)	4.3	$2.01^{+0.22}_{-0.17}$	$15.1^{+8.2}_{-6.4}$	0.89	$0.85^{+1.59}_{-0.85}$	0.46
Mrk 335 (2)	9.7	$2.11^{+0.05}_{-0.04}$	$0.0^{+1.1}_{-0.0}$	0.37	$1.38^{+0.76}_{-0.71}$	0.23
Mrk 335 (3)	6.1	$2.22^{+0.05}_{-0.04}$	$0.0^{+0.8}_{-0.0}$	1.29	$0.56^{+0.75}_{-0.56}$	0.78
Mrk 335 (4)	3.8	$1.85^{+0.21}_{-0.06}$	$0.0^{+6.8}_{-0.0}$	1.03	$0.94^{+1.55}_{-0.94}$	0.65
NGC 526A	1.4	$1.27^{+0.09}_{-0.09}$	$10.0^{+4.9}_{-5.0}$	1.01	$1.21^{+0.38}_{-0.34}$	0.72
Fairall-9	10.2	$1.84^{+0.02}_{-0.02}$	$0.0^{+1.0}_{-0.0}$	1.79	$2.05^{+0.24}_{-0.24}$	1.32
3C111	10.7	$1.77^{+0.04}_{-0.03}$	$18.1^{+1.8}_{-1.3}$	1.35	$1.88^{+0.18}_{-0.18}$	1.11
Akn 120	11.0	$1.81^{+0.03}_{-0.03}$	$0.0^{+0.6}_{-0.0}$	1.50	$0.58^{+0.30}_{-0.30}$	0.43
NGC 2110	9.2	$1.65^{+0.04}_{-0.03}$	$23.5^{+1.8}_{-1.8}$	2.05	$1.64^{+0.17}_{-0.17}$	0.78
NGC 2992	3.8	$1.57^{+0.05}_{-0.06}$	$14.4^{+2.6}_{-2.7}$	4.98	$1.15^{+0.32}_{-0.31}$	1.79
NGC 3227 (1)	10.1	$1.70^{+0.03}_{-0.02}$	$1.3^{+1.1}_{-0.7}$	3.00	$1.22^{+0.16}_{-0.11}$	1.28
NGC 3227 (2)	8.8	$1.63^{+0.03}_{-0.03}$	$3.0^{+1.0}_{-1.0}$	2.99	$1.49^{+0.16}_{-0.15}$	0.69
MCG-5-23-16 (1)	9.5	$1.55^{+0.05}_{-0.03}$	$12.4^{+2.7}_{-1.8}$	2.83	$1.25^{+0.21}_{-0.21}$	0.66
MCG-5-23-16 (2)	3.3	$1.32^{+0.08}_{-0.08}$	$14.8^{+3.9}_{-4.5}$	1.55	$1.47^{+0.37}_{-0.35}$	0.23
NGC 3516 (1)	9.1	$1.73^{+0.09}_{-0.05}$	$52.7^{+6.6}_{-4.0}$	3.50	$0.66^{+0.26}_{-0.24}$	2.07
NGC 3516 (2)	8.5	$1.72^{+0.09}_{-0.06}$	$79.6^{+8.6}_{-5.5}$	2.60	$0.91^{+0.23}_{-0.22}$	0.84
NGC 3516 (3)	8.0	$1.70^{+0.11}_{-0.10}$	$69.5^{+9.7}_{-8.6}$	1.79	$1.08^{+0.33}_{-0.30}$	0.55
NGC 3783	18.6	$1.75^{+0.02}_{-0.02}$	$22.5^{+1.1}_{-1.1}$	6.88	$1.78^{+0.14}_{-0.10}$	0.82
NGC 4051 (1)	3.5	$1.60^{+0.05}_{-0.04}$	$0.0^{+1.9}_{-0.0}$	1.27	$1.08^{+0.44}_{-0.38}$	0.60
NGC 4051 (2)	5.0	$1.73^{+0.05}_{-0.03}$	$2.7^{+1.9}_{-1.4}$	1.17	$1.39^{+0.23}_{-0.23}$	0.72
NGC 4051 (3)	6.7	$1.86^{+0.11}_{-0.08}$	$9.5^{+4.5}_{-3.2}$	1.06	$1.34^{+0.64}_{-0.59}$	0.44
NGC 4593 (1)	5.6	$1.59^{+0.04}_{-0.03}$	$0.5^{+1.5}_{-0.5}$	1.16	$1.43^{+0.19}_{-0.19}$	0.82
NGC 4593 (2)	9.3	$1.73^{+0.03}_{-0.03}$	$0.0^{+0.8}_{-0.0}$	1.89	$0.71^{+0.28}_{-0.28}$	0.48
MCG-6-30-15 (1)	10.0	$1.73^{+0.03}_{-0.03}$	$6.0^{+1.4}_{-1.3}$	6.39	$1.34^{+0.11}_{-0.11}$	0.77
MCG-6-30-15 (2)	18.5	$1.88^{+0.02}_{-0.02}$	$1.7^{+0.8}_{-0.6}$	3.67	$1.76^{+0.14}_{-0.14}$	1.08
MCG-6-30-15 (3)	24.4	$1.88^{+0.02}_{-0.01}$	$1.9^{+0.6}_{-0.4}$	8.52	$1.53^{+0.09}_{-0.10}$	0.82
IC4329A	39.1	$1.84^{+0.01}_{-0.01}$	$2.4^{+0.4}_{-0.3}$	8.15	$1.69^{+0.08}_{-0.06}$	0.49
NGC 5506	31.6	$1.85^{+0.02}_{-0.02}$	$31.6^{+1.1}_{-1.0}$	7.24	$1.27^{+0.11}_{-0.08}$	0.60
NGC 5548 (1)	10.2	$1.70^{+0.01}_{-0.01}$	$0.0^{+0.5}_{-0.0}$	1.84	$1.39^{+0.15}_{-0.14}$	0.35
NGC 5548 (2)	5.0	$1.42^{+0.08}_{-0.07}$	$11.8^{+3.9}_{-3.5}$	1.21	$1.23^{+0.36}_{-0.32}$	0.51

Table 3 – *continued*

Name	A	Γ_{2-18}	N_H	χ^2_ν	Γ_{10-18}	χ^2_ν
NGC 5548 (3)	10.2	$1.55^{+0.03}_{-0.02}$	$4.0^{+1.3}_{-0.9}$	1.81	$1.46^{+0.17}_{-0.17}$	0.43
NGC 5548 (4)	11.1	$1.64^{+0.04}_{-0.03}$	$2.4^{+1.5}_{-1.1}$	1.30	$1.53^{+0.17}_{-0.17}$	0.27
NGC 5548 (5)	15.3	$1.73^{+0.03}_{-0.02}$	$1.7^{+1.0}_{-0.7}$	2.41	$1.74^{+0.16}_{-0.12}$	0.44
NGC 5548 (6)	10.7	$1.70^{+0.02}_{-0.02}$	$0.6^{+0.8}_{-0.6}$	2.68	$1.26^{+0.14}_{-0.13}$	1.19
NGC 5548 (7)	7.3	$1.64^{+0.04}_{-0.02}$	$0.0^{+1.4}_{-0.0}$	1.30	$1.31^{+0.26}_{-0.24}$	0.80
NGC 5548 (8)	12.3	$1.68^{+0.01}_{-0.01}$	$0.0^{+0.5}_{-0.0}$	1.99	$1.48^{+0.15}_{-0.15}$	0.97
NGC 5548 (9)	5.1	$1.56^{+0.06}_{-0.04}$	$0.7^{+2.2}_{-0.7}$	1.22	$1.89^{+0.29}_{-0.28}$	0.77
NGC 5548 (10)	4.9	$1.65^{+0.02}_{-0.02}$	$0.0^{+0.8}_{-0.0}$	1.81	$1.45^{+0.26}_{-0.26}$	0.62
NGC 5548 (11)	6.1	$1.70^{+0.04}_{-0.03}$	$0.0^{+1.5}_{-0.0}$	1.32	$1.24^{+0.33}_{-0.32}$	0.48
Mrk 841 (1)	2.3	$1.63^{+0.13}_{-0.09}$	$5.5^{+5.4}_{-3.7}$	1.41	$2.23^{+0.78}_{-0.71}$	0.33
Mrk 841 (2)	1.7	$1.57^{+0.13}_{-0.12}$	$0.0^{+4.8}_{-0.0}$	0.82	$2.03^{+2.09}_{-1.58}$	0.77
3C 382 (1)	2.7	$1.54^{+0.08}_{-0.08}$	$2.1^{+3.4}_{-2.1}$	1.09	$2.11^{+0.56}_{-0.43}$	0.45
3C 382 (2)	2.6	$1.53^{+0.07}_{-0.05}$	$0.0^{+2.9}_{-0.0}$	0.83	$2.08^{+0.67}_{-0.61}$	0.33
3C 382 (3)	2.3	$1.46^{+0.04}_{-0.04}$	$0.0^{+1.4}_{-0.0}$	1.06	$1.58^{+0.38}_{-0.34}$	0.20
3C 390.3	14.7	$1.80^{+0.01}_{-0.01}$	$0.0^{+0.3}_{-0.0}$	2.29	$1.48^{+0.11}_{-0.11}$	0.98
Mrk 509 (1)	18.8	$1.85^{+0.01}_{-0.01}$	$0.0^{+0.2}_{-0.0}$	5.24	$1.27^{+0.17}_{-0.12}$	0.74
Mrk 509 (2)	13.9	$1.74^{+0.01}_{-0.02}$	$0.0^{+0.2}_{-0.0}$	3.30	$1.47^{+0.15}_{-0.15}$	0.29
Mrk 509 (3)	12.7	$1.77^{+0.01}_{-0.01}$	$0.0^{+0.2}_{-0.0}$	2.36	$1.53^{+0.15}_{-0.15}$	0.68
Mrk 509 (4)	13.8	$1.74^{+0.02}_{-0.02}$	$0.0^{+0.2}_{-0.0}$	1.52	$1.94^{+0.19}_{-0.18}$	0.40
H2106-099 (1)	4.2	$1.84^{+0.05}_{-0.04}$	$0.0^{+0.9}_{-0.0}$	1.47	$1.36^{+0.50}_{-0.46}$	0.80
H2106-099 (2)	3.8	$1.88^{+0.06}_{-0.05}$	$0.0^{+1.4}_{-0.0}$	0.58	$0.58^{+0.67}_{-0.58}$	0.39
NGC 7172	21.7	$1.80^{+0.03}_{-0.02}$	$103.2^{+3.8}_{-2.4}$	2.08	$1.52^{+0.11}_{-0.07}$	1.22
NGC 7213 (1)	8.5	$1.68^{+0.03}_{-0.02}$	$0.8^{+1.3}_{-0.8}$	1.85	$1.72^{+0.24}_{-0.23}$	1.14
NGC 7213 (2)	12.3	$1.80^{+0.03}_{-0.02}$	$1.1^{+1.1}_{-0.8}$	2.04	$2.13^{+0.20}_{-0.19}$	0.41
NGC 7314	7.8	$1.75^{+0.04}_{-0.05}$	$4.3^{+1.7}_{-1.8}$	1.22	$1.35^{+0.25}_{-0.24}$	0.94
NGC 7469	11.5	$1.84^{+0.02}_{-0.02}$	$0.0^{+0.5}_{-0.0}$	2.78	$1.31^{+0.21}_{-0.21}$	0.93
MCG-2-58-22 (1)	3.6	$1.51^{+0.03}_{-0.03}$	$0.0^{+1.0}_{-0.0}$	1.46	$1.53^{+0.24}_{-0.23}$	0.92
MCG-2-58-22 (2)	4.8	$1.55^{+0.09}_{-0.06}$	$3.6^{+4.1}_{-2.8}$	1.20	$0.70^{+0.43}_{-0.39}$	0.61
MCG-2-58-22 (3)	3.0	$1.43^{+0.04}_{-0.03}$	$0.0^{+2.1}_{-0.0}$	1.15	$1.33^{+0.36}_{-0.33}$	0.38
MCG-2-58-22 (4)	5.4	$1.49^{+0.05}_{-0.03}$	$4.5^{+2.1}_{-1.5}$	1.28	$1.41^{+0.21}_{-0.21}$	0.20

[a]Normalizing flux at 1 keV in units of 10^{-3} photon cm^{-2} s^{-1} keV^{-1}. [b]Column density in units of 10^{21} cm^{-2}, 2–18 keV fits. [c]For 24 degrees of freedom, 2–18 keV fits. [d]For 11 degrees of freedom, 10–18 keV fits.

with an intrinsic spread $\sigma_p = 0.15^{+0.04}_{-0.03}$ (68 per cent confidence limits for two interesting parameters). The 99 per cent confidence lower limit for the intrinsic deviation is $\sigma_p > 0.11$, showing that there is indeed a small, but significant, spread of apparent power-law indices (note, however, that this does not necessarily represent true differences in the underlying continuum from object to object, because of the additional complexities in the spectrum – see Section 10).

4.2 10–18 keV: the 'hard tail'

Fig. 3 shows the histogram of spectral indices derived from a higher energy band, 10–18 keV, which are detailed in Table 3, column 6. The reduced χ^2 values for these fits are shown in column 7. Absorption is negligible in this energy range and was excluded from these fits, which gave a flatter average slope, $\overline{\Gamma}_{10-18} = 1.49 \pm 0.03$. From equation (5) an estimate for the mean of the parent population $\langle \Gamma_{10-18} \rangle = 1.45 \pm 0.08$ is obtained, with an intrinsic spread $\sigma_p = 0.22^{+0.08}_{-0.07}$. Statistical tests were carried out to establish whether the measured 2–18 keV (effectively ~2–10 keV) and 10–18 keV indices could have been drawn from the same parent distribution. A Kolmogorov–Smirnov (KS) test implies that the two distributions are significantly different at > 99.9 per cent confidence (the probability of being drawn from the same parent distribution = 0.0005). A χ^2 test comparing the two distributions also shows a significant difference at the > 95 per cent level ($\chi^2 = 26.4/15$ d.o.f.; the probability of obtaining this value by chance = 0.03). Note also that the expectation values for the mean obtained from the maximum-likelihood method (equation 5) are inconsistent at a high confidence level ($\Gamma_{2-18} > 1.61$

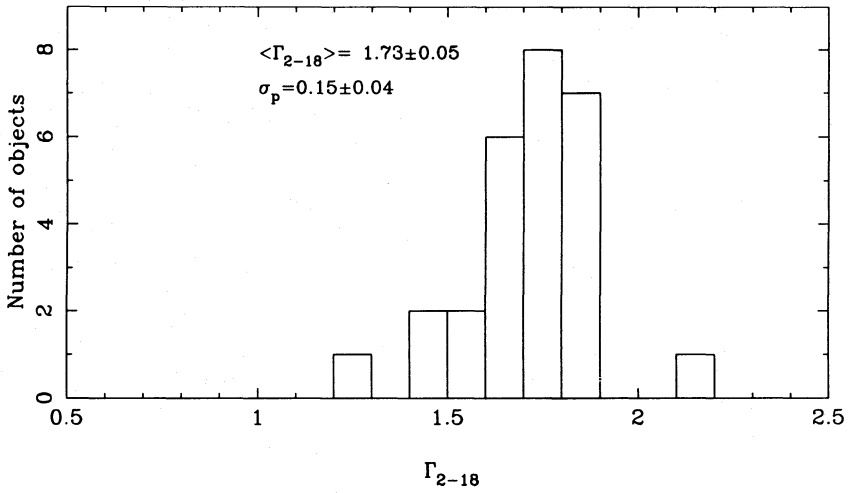

Figure 2. Histogram of the photon indices obtained for a simple power-law plus absorption fit in the 2–18 keV energy range. Although the fits are very poor (see Table 3), the derived photon index is consistent with that observed previously with *HEAO-1* and *EXOSAT*, with a mean value of $\Gamma_{2-18} = 1.73$ and significant intrinsic dispersion 0.15 (see text).

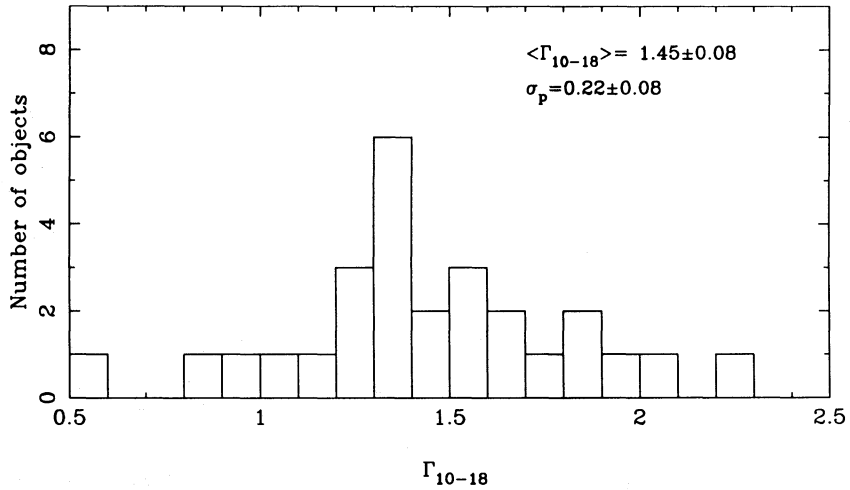

Figure 3. Histogram of the photon indices obtained for a simple power-law fit in the 10–18 keV energy range. Good fits are generally obtained, reflecting the relatively poor statistical quality of the data in this energy range, but the photon indices are found to be significantly flatter than those in the 2–18 keV (effectively 2–10 keV) fits. Here we find a mean value of $\Gamma_{10-18} = 1.45$ with significant dispersion of $\sigma_p = 0.22$. This indicates an additional component to the data, a spectral flattening or 'hard tail'.

and $\Gamma_{10-18} < 1.43$, both at the 99 per cent level). We conclude that the continuum becomes significantly flatter above ~ 10 keV.

The flattening at high energies indicates an additional component to the spectrum, which probably arises from reprocessing in optically thick material close to the central source. This point is addressed further in Sections 8 and 10. The low signal-to-noise ratio above 10 keV makes further, more complex modelling of the higher energy continuum pointless. Therefore we now concentrate on the spectrum covering the full 2–18 keV energy range.

5 ABSORBING COLUMN DENSITY

HEAO-1 and *EXOSAT* both found absorption in some low-luminosity AGN, in simple power-law fits in the 2–10 keV range. The histogram of N_H values obtained from the 2–18 keV simple power-law fits to the *Ginga* data is shown in Fig. 4. The LAC detector is sensitive to columns $>$few $\times 10^{21}$ cm^{-2}. Roughly half the sources show a significantly detected column (see Table 3) above the Galactic value, which is typically $\sim$few $\times 10^{20}$ cm^{-2} (Stark et al. 1992) and therefore negligible in the *Ginga* band. Absorption at 2–3 keV is apparently rather common in this low-luminosity AGN sample. The very similar *EXOSAT* sample of Turner & Pounds (1989) shows rather less absorption, which is puzzling, as the *EXOSAT* ME plus low-energy (LE) fits went down to 0.1 keV, where absorption should be more evident. We return to this point later, but note here that this strongly suggests that the absorption is complex, and not well approximated by a uniform, neutral absorber as tested against the *EXOSAT* and *HEAO-1* data. Note that the distribution in Fig. 4 is not well approximated by a Gaussian, making the maximum-likelihood analysis invalid.

6 IRON-LINE EMISSION

As many of the power-law fits described in Section 4 gave unacceptable χ^2_ν, a more complex model must be sought. The most prominent deviation from this simple, power-law model, apparent from Fig. 1(a), appears as an excess close to 6.5 keV. This is highly suggestive of a line arising from iron K-shell emission. Fits were therefore conducted, in the 2–18 keV range, including a narrow ($\sigma_{K\alpha} = 0.1$ keV) Gaussian emission component (equation 2). Three fits were tried, one with the line energy fixed at 6.4 keV (the appropriate value for Fe I), one with the line energy fixed at 6.7 keV (Fe XXVI), and one with the line energy as a free parameter (all energies are measured in the rest-frame of the Seyfert nucleus). We have assessed the significance of inclusion of an emission line using the *F*-test (e.g. Bevington 1969). The derived *F*-statistics are shown in columns 7 and 10 of Table 4 for the 6.4- and 6.7-keV lines, respectively. The values of F corresponding to 90, 95 and 99 per cent confidence are 2.93, 4.26 and 7.82, respectively. We see from Table 4 that lines are detected at >99 per cent confidence in 37 of the 60 observations, and in 17 of the 27 objects. Taking the 90 per cent significance level, we find significant detections in all but five of the observations, and only two of the sample sources, Akn 120 and 3C 390.3, show no significant improvement with the addition of an iron line. We note that this last is a radio-loud Seyfert, and is the highest-luminosity source in the sample. The equivalent widths (equation 3) for the two lines are detailed in columns 6 and 9 of Table 4. Where no significant line is detected, we show the 68 per cent upper limit. Although the fits are improved substantially with the addition of an emission line, not all are statistically acceptable; indeed, 19 show $\chi^2_\nu > 1.4$, suggesting even more complexity. However, iron-line emission is clearly an important phenomenon. Therefore we now analyse the properties of the sample iron line in more detail.

6.1 Line energy

Column 12 of Table 4 shows the centroid energy of the emission line in the free fit, and indicates that lines close to 6.4 keV are generally preferred. Indeed, the weighted mean (redshift-corrected) line energy is $\bar{E}_{K\alpha} = 6.37 \pm 0.04$ keV. The

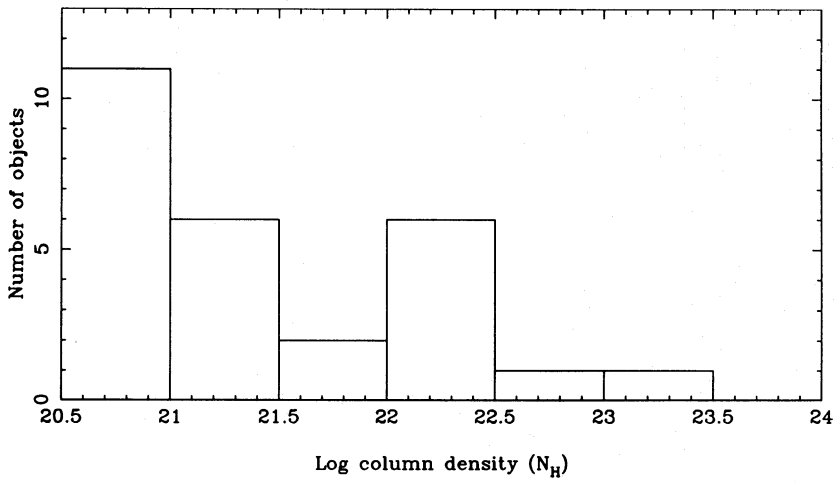

Figure 4. Histogram of the total equivalent hydrogen column density, N_H, derived from simple power-law fits in the 2–18 keV range. Where the best-fitting column density is below $10^{20.5}$ cm^{-2}, the object has been added to the lowest bin in the histogram. Roughly half of the sources have no detected column density in these fits. However, some do show significant absorption at soft X-ray energies, as found with the *HEAO-1* and *EXOSAT* medium-energy spectral fits. The fact that most of these sources are strong in the *EXOSAT* LE range and in *ROSAT* data indicates that the absorption is more complex than a simple, neutral column density.

Table 4. Line fits.

Name	A[a]	Γ^b_{2-18}	N_H[c]	$I^d_{K\alpha}$	$W^e_{K\alpha}$	F^f	χ^{2g}_ν	$W^h_{K\alpha}$	F^i	χ^{2j}_ν	$E^k_{K\alpha}$
Mrk 335 (1)	4.6	$2.07^{+0.32}_{-0.21}$	$15.5^{+11.3}_{-7.8}$	$2.3^{+2.9}_{-2.3}$	< 550	3.0	0.82	< 600	2.4	0.84	–
Mrk 335 (2)	9.9	$2.13^{+0.09}_{-0.05}$	$0.0^{+3.1}_{-0.0}$	$1.8^{+2.7}_{-1.8}$	97 ± 142	5.6	0.31	< 230	2.4	0.35	$6.11^{+2.86}_{-1.92}$
Mrk 335 (3)	6.3	$2.25^{+0.07}_{-0.06}$	$0.0^{+1.7}_{-0.0}$	$1.5^{+1.6}_{-1.5}$	< 330	2.4	1.22	< 350	2.0	1.24	–
Mrk 335 (4)	4.5	$1.94^{+0.28}_{-0.17}$	$0.0^{+8.5}_{-0.0}$	$5.5^{+5.0}_{-5.2}$	454 ± 421	4.5	0.90	227 ± 428	1.0	1.03	$5.99^{+0.55}_{-0.55}$
NGC 526A	1.3	$1.25^{+0.12}_{-0.11}$	$7.8^{+6.4}_{-5.8}$	$2.8^{+1.8}_{-1.8}$	216 ± 142	11.1	0.71	254 ± 151	16.1	0.62	$6.75^{+0.60}_{-0.56}$
Fairall-9	10.4	$1.86^{+0.03}_{-0.02}$	$0.0^{+1.4}_{-0.0}$	$3.9^{+1.8}_{-1.8}$	118 ± 54	14.7	1.14	154 ± 59	29.4	0.82	$6.86^{+0.30}_{-0.32}$
3C111	10.8	$1.78^{+0.04}_{-0.04}$	$18.2^{+2.0}_{-1.8}$	$1.3^{+1.8}_{-1.3}$	< 80	1.4	1.33	56 ± 50	3.6	1.22	$7.37^{+1.18}_{-0.87}$
AKN120	11.1	$1.82^{+0.04}_{-0.04}$	$0.0^{+0.9}_{-0.0}$	$3.4^{+3.8}_{-3.4}$	< 190	1.8	1.45	< 220	2.7	1.40	–
NGC 2110	9.2	$1.67^{+0.05}_{-0.04}$	$22.8^{+2.3}_{-2.2}$	$6.6^{+2.1}_{-2.1}$	165 ± 52	55.1	0.63	170 ± 56	44.4	0.73	$6.49^{+0.26}_{-0.25}$
NGC 2992	4.0	$1.64^{+0.08}_{-0.08}$	$13.6^{+3.3}_{-3.3}$	$8.2^{+1.6}_{-1.6}$	438 ± 88	55.1	1.53	433 ± 95	33.6	2.11	$6.43^{+0.16}_{-0.16}$
MCG-5-23-16 (1)	9.5	$1.57^{+0.06}_{-0.05}$	$11.5^{+3.0}_{-2.6}$	$11.9^{+3.6}_{-3.6}$	238 ± 72	29.2	1.30	245 ± 76	26.2	1.38	$6.48^{+0.28}_{-0.26}$
MCG-5-23-16 (2)	3.1	$1.32^{+0.10}_{-0.10}$	$12.0^{+5.6}_{-5.8}$	$9.3^{+3.5}_{-3.5}$	351 ± 132	44.6	0.55	392 ± 139	67.7	0.41	$6.65^{+0.29}_{-0.29}$
NGC 3227 (1)	10.3	$1.73^{+0.04}_{-0.03}$	$1.4^{+1.4}_{-1.0}$	$5.5^{+1.8}_{-1.7}$	133 ± 42	23.8	1.54	137 ± 44	20.4	1.66	$6.50^{+0.23}_{-0.23}$
NGC 3227 (2)	9.1	$1.66^{+0.04}_{-0.03}$	$3.0^{+1.4}_{-1.2}$	$7.3^{+1.8}_{-1.8}$	176 ± 44	87.4	0.65	166 ± 47	35.3	1.23	$6.38^{+0.18}_{-0.19}$
NGC 3516 (1)	8.6	$1.74^{+0.11}_{-0.08}$	$48.7^{+7.7}_{-5.4}$	$9.6^{+3.0}_{-3.2}$	303 ± 99	14.2	2.26	282 ± 105	10.3	2.52	$6.43^{+0.24}_{-0.23}$
NGC 3516 (2)	7.5	$1.68^{+0.09}_{-0.09}$	$71.9^{+8.7}_{-8.5}$	$8.3^{+2.7}_{-2.7}$	283 ± 92	23.9	1.33	221 ± 94	10.0	1.89	$6.22^{+0.24}_{-0.24}$
NGC 3516 (3)	6.8	$1.65^{+0.14}_{-0.12}$	$60.2^{+11.9}_{-10.1}$	$9.5^{+3.7}_{-3.8}$	334 ± 131	23.2	0.93	239 ± 134	7.9	1.39	$6.19^{+0.27}_{-0.28}$
NGC 3783	18.8	$1.77^{+0.03}_{-0.03}$	$21.8^{+1.5}_{-1.4}$	$12.4^{+2.3}_{-2.3}$	184 ± 34	35.6	2.82	159 ± 36	15.2	4.32	$6.22^{+0.14}_{-0.15}$
NGC 4051 (1)	3.6	$1.63^{+0.07}_{-0.06}$	$0.0^{+2.6}_{-0.0}$	$3.1^{+2.3}_{-2.4}$	174 ± 134	5.5	1.07	174 ± 142	5.0	1.09	$6.46^{+0.74}_{-0.77}$
NGC 4051 (2)	5.1	$1.74^{+0.07}_{-0.05}$	$2.8^{+2.3}_{-1.8}$	$1.8^{+1.5}_{-1.4}$	89 ± 73	5.7	0.98	< 150	2.8	1.09	$6.12^{+0.72}_{-0.72}$
NGC 4051 (3)	7.1	$1.90^{+0.15}_{-0.11}$	$9.9^{+5.4}_{-4.4}$	$3.1^{+3.3}_{-3.1}$	154 ± 162	3.5	0.96	< 310	2.2	1.01	$5.51^{+0.60}_{-0.49}$
NGC 4593 (1)	5.6	$1.60^{+0.05}_{-0.03}$	$0.2^{+2.0}_{-0.2}$	$3.1^{+1.8}_{-1.8}$	107 ± 63	13.2	0.77	118 ± 68	14.1	0.75	$6.57^{+0.40}_{-0.41}$
NGC 4593 (2)	9.5	$1.75^{+0.04}_{-0.04}$	$0.0^{+1.2}_{-0.0}$	$4.6^{+3.6}_{-3.5}$	124 ± 95	3.7	1.70	123 ± 104	3.1	1.74	$6.53^{+0.47}_{-0.48}$
MCG-6-30-15 (1)	9.5	$1.72^{+0.04}_{-0.03}$	$4.4^{+2.0}_{-1.4}$	$9.6^{+2.1}_{-2.2}$	250 ± 55	20.0	3.57	199 ± 57	8.7	4.84	$6.19^{+0.16}_{-0.20}$
MCG-6-30-15 (2)	19.4	$1.91^{+0.03}_{-0.02}$	$2.1^{+1.1}_{-0.8}$	$8.3^{+2.0}_{-1.9}$	149 ± 36	60.1	1.06	130 ± 39	20.6	2.02	$6.29^{+0.17}_{-0.16}$
MCG-6-30-15 (3)	25.4	$1.91^{+0.02}_{-0.01}$	$2.2^{+0.7}_{-0.5}$	$9.0^{+1.8}_{-1.7}$	124 ± 24	21.8	4.56	106 ± 27	10.0	6.19	$6.18^{+0.14}_{-0.20}$
IC4329A	40.4	$1.86^{+0.01}_{-0.01}$	$2.7^{+0.4}_{-0.5}$	$13.9^{+2.1}_{-2.1}$	110 ± 16	81.0	1.88	106 ± 18	33.7	3.45	$6.37^{+0.12}_{-0.11}$
NGC 5506	31.5	$1.86^{+0.03}_{-0.02}$	$30.7^{+1.6}_{-1.0}$	$15.1^{+2.8}_{-2.8}$	161 ± 30	38.0	2.85	148 ± 31	20.5	3.99	$6.39^{+0.13}_{-0.12}$
NGC 5548 (1)	10.4	$1.71^{+0.02}_{-0.02}$	$0.0^{+0.7}_{-0.0}$	$3.4^{+1.8}_{-1.9}$	78 ± 42	8.5	1.40	73 ± 46	5.7	1.54	$6.36^{+0.43}_{-0.40}$
NGC 5548 (2)	4.9	$1.43^{+0.10}_{-0.09}$	$10.3^{+4.9}_{-4.2}$	$8.1^{+3.8}_{-3.8}$	239 ± 111	27.9	0.57	202 ± 119	12.0	0.83	$6.22^{+0.35}_{-0.32}$
NGC 5548 (3)	10.5	$1.57^{+0.04}_{-0.03}$	$4.2^{+1.5}_{-1.2}$	$5.7^{+2.4}_{-2.4}$	101 ± 43	19.2	1.03	92 ± 48	10.4	1.30	$6.14^{+0.44}_{-0.49}$
NGC 5548 (4)	11.3	$1.66^{+0.04}_{-0.04}$	$2.3^{+1.7}_{-1.5}$	$6.1^{+2.7}_{-2.6}$	118 ± 52	31.7	0.57	102 ± 56	12.9	0.87	$6.29^{+0.32}_{-0.36}$
NGC 5548 (5)	15.8	$1.76^{+0.03}_{-0.02}$	$1.8^{+1.1}_{-0.9}$	$7.4^{+2.1}_{-2.1}$	123 ± 35	68.8	0.63	116 ± 39	29.6	1.10	$6.32^{+0.24}_{-0.23}$
NGC 5548 (6)	10.9	$1.72^{+0.03}_{-0.03}$	$0.7^{+1.0}_{-0.7}$	$3.9^{+1.6}_{-1.6}$	87 ± 36	10.7	1.91	82 ± 39	6.8	2.16	$6.37^{+0.29}_{-0.31}$
NGC 5548 (7)	7.4	$1.66^{+0.05}_{-0.03}$	$0.0^{+1.9}_{-0.0}$	$4.4^{+2.5}_{-2.5}$	128 ± 73	12.1	0.89	137 ± 80	11.3	0.91	$6.53^{+0.41}_{-0.46}$
NGC 5548 (8)	12.5	$1.69^{+0.02}_{-0.02}$	$0.0^{+0.7}_{-0.0}$	$4.4^{+2.3}_{-2.3}$	82 ± 42	8.6	1.51	68 ± 46	4.4	1.74	$6.07^{+0.44}_{-0.50}$
NGC 5548 (9)	5.2	$1.59^{+0.07}_{-0.05}$	$0.7^{+2.6}_{-0.7}$	$4.4^{+2.2}_{-2.2}$	164 ± 81	22.8	0.64	169 ± 88	18.2	0.71	$6.47^{+0.40}_{-0.43}$
NGC 5548 (10)	5.1	$1.68^{+0.04}_{-0.03}$	$0.0^{+1.1}_{-0.0}$	$3.9^{+1.8}_{-1.7}$	173 ± 77	15.8	1.12	190 ± 85	15.4	1.13	$6.53^{+0.38}_{-0.37}$
NGC 5548 (11)	6.2	$1.72^{+0.07}_{-0.04}$	$0.0^{+2.1}_{-0.0}$	$3.9^{+2.6}_{-2.5}$	151 ± 99	8.1	1.02	188 ± 109	11.8	0.91	$6.74^{+0.51}_{-0.50}$
Mrk 841 (1)	2.4	$1.71^{+0.18}_{-0.13}$	$5.4^{+6.5}_{-5.1}$	$4.5^{+1.9}_{-1.8}$	447 ± 184	37.4	0.56	377 ± 194	15.0	0.89	$6.29^{+0.30}_{-0.32}$
Mrk 841 (2)	1.8	$1.62^{+0.19}_{-0.16}$	$0.0^{+6.3}_{-0.0}$	$2.4^{+3.2}_{-2.4}$	< 550	2.2	0.78	< 570	0.7	0.83	–
3C382 (1)	2.8	$1.57^{+0.10}_{-0.07}$	$1.7^{+4.0}_{-1.7}$	$4.0^{+1.9}_{-1.9}$	268 ± 129	31.5	0.48	281 ± 137	29.3	0.50	$6.52^{+0.39}_{-0.38}$
3C382 (2)	2.7	$1.58^{+0.09}_{-0.07}$	$0.0^{+3.4}_{-0.0}$	$4.1^{+2.3}_{-2.3}$	290 ± 160	32.3	0.36	291 ± 171	23.3	0.43	$6.44^{+0.49}_{-0.45}$
3C382 (3)	2.4	$1.50^{+0.05}_{-0.05}$	$0.0^{+1.8}_{-0.0}$	$3.0^{+1.6}_{-1.6}$	202 ± 108	21.6	0.57	212 ± 116	20.1	0.59	$6.53^{+0.47}_{-0.43}$
3C390.3	14.7	$1.80^{+0.01}_{-0.01}$	$0.0^{+0.5}_{-0.0}$	$1.1^{+1.6}_{-1.1}$	< 55	0.8	2.31	< 55	0.6	2.33	–
Mrk 509 (1)	19.1	$1.86^{+0.02}_{-0.02}$	$0.0^{+0.4}_{-0.0}$	$5.3^{+2.5}_{-2.6}$	89 ± 43	3.0	4.83	99 ± 46	3.5	4.75	$6.61^{+0.34}_{-0.32}$
Mrk 509 (2)	14.0	$1.75^{+0.02}_{-0.02}$	$0.0^{+0.3}_{-0.0}$	$2.2^{+2.6}_{-2.2}$	< 90	0.7	3.34	< 85	0.4	3.38	–
Mrk 509 (3)	12.8	$1.79^{+0.02}_{-0.02}$	$0.0^{+0.3}_{-0.0}$	$3.8^{+1.9}_{-1.9}$	81 ± 41	7.5	1.86	80 ± 44	6.2	1.94	$6.42^{+0.45}_{-0.41}$
Mrk 509 (4)	14.0	$1.75^{+0.02}_{-0.02}$	$0.0^{+0.3}_{-0.0}$	$3.5^{+2.6}_{-2.7}$	65 ± 49	4.6	1.32	77 ± 53	5.7	1.27	$6.65^{+0.64}_{-0.56}$
H2106-099 (1)	4.2	$1.84^{+0.06}_{-0.06}$	$0.0^{+1.2}_{-0.0}$	$0.0^{+2.0}_{-0.0}$	< 140	0.1	1.53	< 180	0.1	1.53	–
H2106-099 (2)	3.9	$1.91^{+0.10}_{-0.08}$	$0.0^{+2.5}_{-0.0}$	$1.7^{+2.1}_{-1.7}$	149 ± 189	4.3	0.51	156 ± 205	4.3	0.51	$6.51^{+1.42}_{-1.01}$
NGC 7172	20.5	$1.78^{+0.05}_{-0.03}$	$100.0^{+5.2}_{-3.3}$	$4.5^{+2.3}_{-2.7}$	71 ± 39	6.2	1.71	63 ± 38	5.4	1.76	$6.44^{+0.49}_{-0.46}$
NGC 7213 (1)	8.7	$1.70^{+0.05}_{-0.04}$	$0.8^{+1.8}_{-0.8}$	$5.2^{+2.3}_{-2.3}$	141 ± 63	14.3	1.19	155 ± 69	14.9	1.17	$6.58^{+0.34}_{-0.39}$
NGC 7213 (2)	12.9	$1.83^{+0.04}_{-0.04}$	$1.5^{+1.3}_{-1.2}$	$5.8^{+2.0}_{-2.0}$	134 ± 47	31.4	0.90	171 ± 52	81.2	0.47	$6.78^{+0.23}_{-0.24}$
NGC 7314	7.9	$1.76^{+0.06}_{-0.06}$	$4.2^{+2.3}_{-2.2}$	$3.3^{+2.3}_{-2.3}$	110 ± 76	7.5	0.96	< 170	3.9	1.09	$6.03^{+0.66}_{-0.65}$
NGC 7469	11.7	$1.85^{+0.03}_{-0.03}$	$0.0^{+0.7}_{-0.0}$	$3.5^{+2.4}_{-2.3}$	94 ± 63	3.1	2.56	98 ± 70	2.8	2.59	$6.47^{+0.59}_{-0.49}$
MCG-2-58-22 (1)	3.7	$1.53^{+0.04}_{-0.04}$	$0.0^{+1.1}_{-0.0}$	$2.7^{+1.7}_{-1.7}$	125 ± 80	7.5	1.15	145 ± 86	9.1	1.09	$6.85^{+0.87}_{-0.77}$
MCG-2-58-22 (2)	4.9	$1.57^{+0.11}_{-0.09}$	$3.3^{+4.5}_{-3.3}$	$4.3^{+3.2}_{-3.3}$	163 ± 122	6.4	0.98	154 ± 130	4.7	1.04	$6.27^{+0.88}_{-0.88}$
MCG-2-58-22 (3)	3.1	$1.46^{+0.05}_{-0.05}$	$0.0^{+2.4}_{-0.0}$	$4.1^{+2.1}_{-2.1}$	200 ± 101	22.2	0.61	224 ± 109	26.3	0.56	$6.63^{+0.42}_{-0.45}$
MCG-2-58-22 (4)	5.5	$1.50^{+0.05}_{-0.05}$	$4.1^{+2.3}_{-2.0}$	$4.5^{+2.0}_{-2.0}$	136 ± 61	29.1	0.59	120 ± 66	14.0	0.83	$6.16^{+0.43}_{-0.46}$

[a]Power-law flux at 1 keV, in units of 10^{-3} photon cm^{-2} s^{-1} keV^{-1}. [b]Power-law photon index. [c]Neutral column density in units of 10^{21} cm^{-2}. [d]Intensity of the 6.4-keV emission line in units of 10^{-4} photon cm^{-2} s^{-1}. [e]Equivalent width of the 6.4-keV emission line (eV). [f]F-statistic for one additional parameter (6.4-keV line). [g]For 23 degrees of freedom, 6.4-keV line. [h]Equivalent width of 6.7-keV emission line (eV). [i]F-statistic for one additional parameter (6.7-keV line). [j]For 23 degrees of freedom, 6.7-keV line. [k]Line energy (free fit).

expectation value obtained from equation (5) is $\langle E_{K\alpha}\rangle = 6.37^{+0.07}_{-0.06}$, close to the value for neutral iron. Fig. 5 shows the distribution of line energies, which is strongly peaked near 6.4 keV. The histogram indicates a spread of values about this mean. However, the bulk of this may be purely statistical. Formally, a limit of $\sigma_p < 0.23$ can be placed at 99 per cent confidence, with no significant detection of an intrinsic spread. A constant fit to the line energies gives $\chi^2_\nu = 0.67/24$ d.o.f., further supporting the hypothesis that the bulk of the sources are consistent with the mean line energy. A similarly good fit, $\chi^2_\nu = 0.66$, is obtained for the hypothesis of a constant line energy of 6.4 keV, the value expected from fluorescence by cold iron. Thermal line emission from hot plasmas, as is observed in, e.g., clusters of galaxies and supernova remnants, would be expected at a higher energy ~6.7–6.9 keV, depending on the temperature of the emitting gas. Line emission at 6.7 keV is excluded as a unique value by these data at the >99 per cent level ($\chi^2_\nu = 3.56$). We note, however, that a warm line *is* preferred in a minority of sources (see, e.g., Fairall-9 and NGC 7213).

6.2 Equivalent width

The weighted mean of the narrow-line equivalent widths is $\overline{W}_{K\alpha} = 127 \pm 7$ eV (equation 3; $\langle W_{K\alpha}\rangle = 140 \pm 20$ eV, equation 5), for the (preferred) line energy of 6.4 keV. The histogram, for a fit in which the energy has been fixed at 6.4 keV and the width at 0.1 keV, is shown in Fig. 6 and peaks around ~100–150 eV, the prevailing value for the bulk of sources. However, the histogram has a significant intrinsic spread at

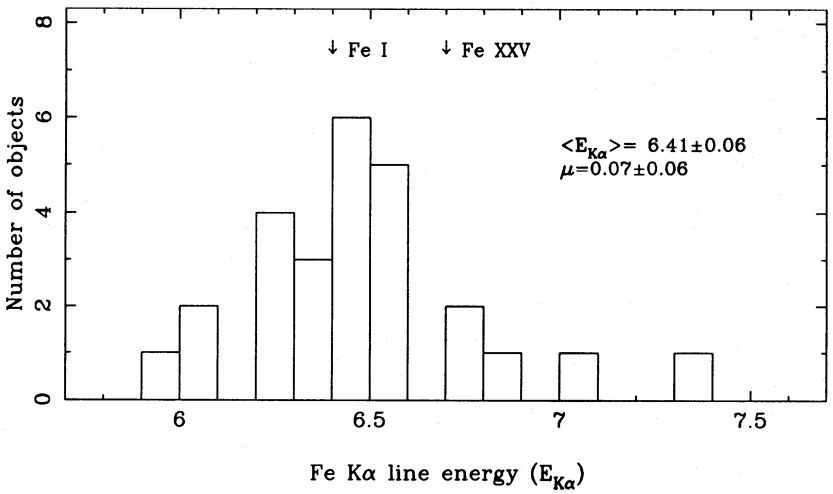

Figure 5. Histogram of the derived line energies $E_{K\alpha}$ for a narrow ($\sigma_{K\alpha} = 0.1$ keV) Gaussian emission feature. In the rest-frame of the source, the mean energy is $E_{K\alpha} = 6.37$ keV, close to the value expected from neutral iron (6.4 keV). The distribution is consistent with no significant intrinsic spread. In a few individual cases a higher line-energy may be preferred, however.

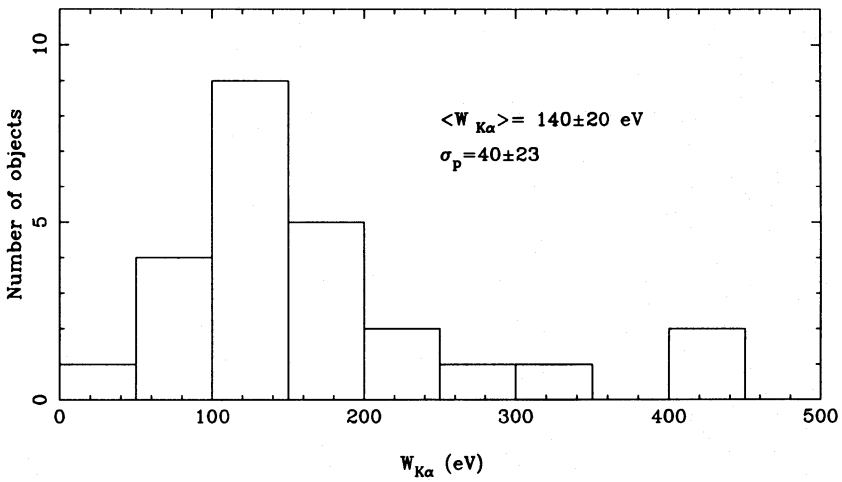

Figure 6. Histogram of the line equivalent widths ($W_{K\alpha}$) obtained from a fit with a power law and narrow ($\sigma_{K\alpha} = 0.1$) Gaussian at an energy of 6.4 keV. The mean value for our sample is found to be ~140 eV. There is an apparent spread of values, with some individual sources showing much larger equivalent widths. Note that when a more realistic continuum model is applied, the mean equivalent width is found to be closer to 110 eV. None the less, these values imply extremely high columns and covering fractions for the line-emitting material, which must therefore lie out of the line of sight, as otherwise the soft X-rays would be extinguished.

~95 per cent confidence, $\sigma_p = 39^{+29}_{-16}$ eV (but see Section 10). The 'canonical' equivalent width of ~150 eV implies columns of $>10^{23}$ cm^{-2} for spherical covering. In contrast, the 'typical' apparent cold absorption columns (Fig. 4) of $N_H \sim 10^{21-22}$ cm^{-2} can produce only ~a few ×10 eV of line emission (see Section 8).

6.3 Broad lines

16 of the 60 spectra show a significant improvement in the fit (at the >95 per cent level) when the line width ($\sigma_{K\alpha}$ in equation 2) is left as a free parameter. However, some of the fits thus obtained are unrealistic, with several observations with low signal-to-noise ratio showing extremely broad lines, which account for much of the continuum flux. We exclude these from further discussion, leaving eight observations (six objects) with typical widths of order $\sigma_{K\alpha} \sim 0.9$ keV (corresponding to Doppler broadening at $<10R_s$ if Keplerian motions apply). The fits are detailed in Table 5. Few of the fits can exclude a line width of this order, even in the best-determined cases. This is due to the finite resolution of the LAC detector. The broadening could arise from Doppler motions, gravity, electron scattering or ionization blends, although these processes may also shift the peak energy, and such effects must be reconciled with the mean energy. In addition, poor modelling of the continuum could result in a spurious 'broad emission line'. As we now know, the X-ray continuum in the 2–20 keV band is more complex than the simple power-law model assumed thus far. We must therefore treat with caution the above line profiles. In particular, with the exception of 3C 111 which may have an unrealistically high line-energy, all of the sources with apparently broad emission lines show evidence for a 'warm absorber' (see Section 9), which could significantly affect the continuum parametrization around the line.

7 IRON ABSORPTION FEATURES

As stated in the introduction, absorption edges, sometimes at a higher energy than the 7.1 keV expected for neutral iron, have been reported for some individual sources. To test for the presence of such a feature, power-law plus absorption-edge fits (equation 4) were carried out for the full sample. As with the line fits, we have tested absorption edges at specific energies: 7.1 keV (the value for cold iron), 8.85 keV (the value for helium-like iron) and 8.0 keV (an intermediate value). A significant improvement, at >90 per cent confidence, over the simple power-law fits was found for 36 out of the 60 spectra, compared to 55/60 for the iron emission-line fits. The details of these fits are shown in Table 6. In this table, as in that for the line (Table 4), the 68 per cent confidence upper limit to N_{HFe} is shown where no edge is detected in a given fit. In the cases where a significant improvement is achieved, a further fit with free-edge energy has been undertaken. Generally, the preferred energy is $E_{th} \sim 8$ keV. Fig. 7 shows the histogram of edge energies for the free-edge fits, roughly half of which are statistically acceptable. Typical column densities in the cases where an edge is detected are several ×10^{23} cm^{-2} (see Fig. 7, inset). One limitation of these fits is that, given the overwhelming evidence for iron Kα emission in these objects, the edge fits may be confused if the emission line is not included in the model. We have therefore repeated the fits including a narrow ($\sigma_{K\alpha} = 0.1$ keV) emission line, fixed at $E_{K\alpha} = 6.4$ keV. In this case we introduce two extra parameters into the fit compared to the power-law plus line model, the energy of the edge and the column density. We restrict the energy to the reasonable range 7.0–10.0 keV. In this case we find a significant improvement over the power-law plus line model for 15 of the 60 fits (11 objects – roughly 40 per cent of the sample) at >90 per cent confidence, with details being shown in Table 7.

Typically, column densities for these fits are $N_{HFe} \sim 10^{23}$ cm^{-2}, slightly *lower* than for the fits without an emission line. This can be seen in Fig. 8, inset. Columns much lower than this are unlikely to be detectable with *Ginga* for observations with signal-to-noise ratios similar to those described here. This can be seen from the typical upper limits in Table 6. The mean energy is $\langle E_{th} \rangle = 7.8 \pm 0.3$ keV, implying that highly ionized material exists in the line of sight. The histogram of edge energies, derived from these fits, is shown in Fig. 8. This shows no significant spread over that expected from the statistical errors ($\sigma_p < 0.82$, at the 99 per cent level). The mean edge energy implies an ionization state ~Fe xx and a temperature ~10^7 K, if the iron is collisionally ionized. This observation strongly suggests that there exist large column densities of hot and/or photoionized medium in the lines of sight to many Seyfert nuclei.

Table 5. Broad-line fits. Only sources in which a significant improvement is found are detailed.

Name	A[a]	Γ^b_{2-18}	N_H[c]	$I^d_{K\alpha}$	$W^e_{K\alpha}$	$E^f_{K\alpha}$	$\sigma^g_{K\alpha}$	F[h]	χ^{2i}_ν
NGC 3783	16.8	$1.74^{+0.05}_{-0.12}$	$18.5^{+2.6}_{-4.7}$	$32.6^{+35.8}_{-12.7}$	448 ± 334	$5.95^{+0.27}_{-0.44}$	$1.04^{+0.62}_{-0.51}$	14.9	1.60
3C 111	11.6	$1.83^{+0.13}_{-0.06}$	$19.0^{+3.4}_{-2.5}$	$8.2^{+22.5}_{-6.0}$	328 ± 567	$8.02^{+1.34}_{-1.01}$	$1.35^{+2.29}_{-1.05}$	6.9	0.90
NGC 5548 (3)	10.3	$1.58^{+0.05}_{-0.08}$	$3.5^{+2.0}_{-3.0}$	$12.1^{+18.0}_{-6.4}$	200 ± 201	$6.02^{+0.48}_{-0.56}$	$0.81^{+0.97}_{-0.51}$	12.3	0.66
NGC 5548 (5)	15.7	$1.76^{+0.04}_{-0.04}$	$1.7^{+1.4}_{-1.3}$	$10.2^{+6.7}_{-4.6}$	165 ± 92	$6.27^{+0.31}_{-0.32}$	$0.53^{+0.58}_{-0.53}$	5.2	0.52
MCG-2-58-22 (4)	5.0	$1.47^{+0.08}_{-0.11}$	$1.9^{+3.9}_{-1.9}$	$11.9^{+31.7}_{-6.6}$	332 ± 534	$5.95^{+0.69}_{-0.97}$	$1.00^{+1.51}_{-0.87}$	18.7	0.31
MCG-5-23-16 (1)	8.8	$1.56^{+0.09}_{-0.27}$	$9.1^{+3.8}_{-9.1}$	$28.3^{+93.3}_{-14.2}$	571 (< 1400)	$6.28^{+0.52}_{-1.02}$	$1.06^{+1.50}_{-0.69}$	8.9	0.97
MCG-6-30-15 (1)	7.7	$1.65^{+0.05}_{-0.03}$	$0.0^{+2.4}_{-0.0}$	$30.2^{+11.6}_{-9.7}$	665 ± 235	$5.59^{+0.29}_{-0.30}$	$1.10^{+0.32}_{-0.26}$	15.1	2.06
MCG-6-30-15 (3)	25.1	$1.92^{+0.03}_{-0.02}$	$1.7^{+1.2}_{-0.8}$	$18.8^{+8.0}_{-5.6}$	230 ± 83	$5.95^{+0.24}_{-0.23}$	$0.82^{+0.32}_{-0.28}$	9.3	3.13

[a]Power-law flux at 1 keV, in units of 10^{-3} photon cm^{-2} s^{-1} keV^{-1}. [b]Power-law photon index. [c]Neutral column density, in units of 10^{21} cm^{-2}. [d]Intensity of the emission line in units of 10^{-4} photon cm^{-2} s^{-1}. [e]Equivalent width of the emission line (eV). [f]Energy of the emission line (keV). [g]1σ width of the Gaussian line (keV). [h]*F*-statistic for the additional parameter ($\sigma_{K\alpha}$). [i]For 22 degrees of freedom.

Table 6. Absorption-edge fits.

Name	A[a]	Γ^{b}_{2-18}	$N_{\rm H}{}^{c}$	$N_{\rm HFe}{}^{d}$	F^{e}	χ^{2f}_{ν}	$N_{\rm HFe}{}^{g}$	F^{h}	χ^{2i}_{ν}	$N_{\rm HFe}{}^{j}$	F^{k}	χ^{2l}_{ν}	$E^{m}_{\rm th}$
Mrk 335 (1)	2.9	$1.76^{+0.34}_{-0.28}$	$9.3^{+10.7}_{-8.7}$	408^{+430}_{-380}	5.9	0.74	765^{+752}_{-548}	12.6	0.60	805^{+898}_{-711}	6.7	0.72	$7.58^{+1.40}_{-0.61}$
Mrk 335 (2)	9.6	$2.11^{+0.07}_{-0.06}$	$0.0^{+2.8}_{-0.0}$	< 160	0.0	0.39	< 320	2.4	0.35	< 400	1.0	0.37	–
Mrk 335 (3)	6.1	$2.22^{+0.06}_{-0.06}$	$0.0^{+1.5}_{-0.0}$	< 130	0.0	1.35	< 260	0.0	1.35	< 330	0.0	1.35	–
Mrk 335 (4)	3.7	$1.76^{+0.23}_{-0.20}$	$0.0^{+4.9}_{-0.0}$	< 810	2.5	0.97	494^{+658}_{-494}	3.9	0.92	< 1300	2.5	0.97	$8.00^{+2.71}_{-2.22}$
NGC 526a	1.4	$1.24^{+0.13}_{-0.14}$	$9.3^{+6.7}_{-6.1}$	< 180	0.3	1.04	224^{+178}_{-171}	7.7	0.79	194^{+243}_{-194}	3.1	0.93	$8.03^{+6.49}_{-8.03}$
Fairall 9	10.2	$1.84^{+0.03}_{-0.02}$	$0.0^{+0.9}_{-0.0}$	< 45	0.0	1.86	< 150	2.0	1.72	< 180	1.4	1.76	–
3C 111	10.8	$1.77^{+0.05}_{-0.03}$	$18.2^{+2.1}_{-1.7}$	< 22	0.0	1.41	< 40	0.0	1.41	< 110	0.1	1.40	–
Akn 120	11.0	$1.81^{+0.04}_{-0.05}$	$0.0^{+0.9}_{-0.0}$	< 100	-0.1	1.57	< 220	2.2	1.43	< 240	1.7	1.46	–
NGC 2110	8.9	$1.64^{+0.05}_{-0.06}$	$23.1^{+2.4}_{-2.5}$	< 80	0.4	2.10	146^{+81}_{-74}	8.3	1.57	182^{+99}_{-95}	8.1	1.58	$8.23^{+2.04}_{-0.42}$
NGC 2992	3.4	$1.49^{+0.09}_{-0.09}$	$12.4^{+3.6}_{-3.3}$	< 220	1.1	4.96	507^{+158}_{-153}	13.1	3.31	529^{+193}_{-178}	8.5	3.79	$7.98^{+0.53}_{-0.28}$
MCG-5-23-16 (1)	9.0	$1.52^{+0.09}_{-0.06}$	$11.6^{+3.5}_{-2.4}$	< 130	0.6	2.88	275^{+99}_{-110}	13.5	1.86	346^{+123}_{-128}	17.2	1.69	$8.49^{+1.00}_{-0.56}$
MCG-5-23-16 (2)	3.4	$1.32^{+0.10}_{-0.11}$	$15.0^{+5.8}_{-5.8}$	< 80	0.0	1.62	259^{+182}_{-180}	5.8	1.29	360^{+237}_{-213}	8.8	1.17	$8.47^{+1.37}_{-0.61}$
NGC 3227 (1)	9.4	$1.65^{+0.04}_{-0.03}$	$0.3^{+1.3}_{-0.3}$	83^{+41}_{-47}	4.4	2.63	164^{+51}_{-52}	19.1	1.71	162^{+61}_{-69}	8.6	2.28	$8.00^{+0.52}_{-0.86}$
NGC 3227 (2)	8.2	$1.58^{+0.05}_{-0.04}$	$1.9^{+1.5}_{-1.3}$	73^{+46}_{-48}	3.0	2.76	176^{+70}_{-64}	13.1	1.99	165^{+85}_{-78}	6.3	2.45	$7.72^{+0.68}_{-0.33}$
NGC 3516 (1)	6.7	$1.55^{+0.14}_{-0.09}$	$47.4^{+7.9}_{-5.4}$	255^{+104}_{-113}	6.6	2.83	502^{+140}_{-172}	19.3	1.98	381^{+157}_{-188}	5.0	2.99	$7.72^{+0.39}_{-0.30}$
NGC 3516 (2)	6.7	$1.56^{+0.13}_{-0.09}$	$74.8^{+10.2}_{-7.0}$	209^{+88}_{-99}	9.0	1.95	405^{+126}_{-142}	28.1	1.22	348^{+153}_{-156}	9.2	1.94	$7.94^{+0.40}_{-0.44}$
NGC 3516 (3)	5.7	$1.49^{+0.15}_{-0.14}$	$63.2^{+11.4}_{-10.5}$	295^{+137}_{-130}	17.5	1.06	374^{+191}_{-172}	15.0	1.13	239^{+193}_{-239}	1.8	1.73	$7.49^{+3.28}_{-7.49}$
NGC 3783	16.8	$1.69^{+0.04}_{-0.04}$	$20.8^{+1.5}_{-1.5}$	99^{+36}_{-34}	4.1	6.10	223^{+53}_{-49}	15.0	4.35	236^{+59}_{-75}	8.2	5.30	$8.00^{+0.24}_{-0.25}$
NGC 4051 (1)	3.5	$1.59^{+0.08}_{-0.07}$	$0.0^{+2.5}_{-0.0}$	< 150	0.1	1.32	< 260	1.0	1.27	< 350	1.8	1.23	–
NGC 4051 (2)	4.5	$1.66^{+0.09}_{-0.06}$	$1.2^{+2.6}_{-1.2}$	101^{+73}_{-86}	4.6	1.01	178^{+99}_{-108}	12.7	0.78	165^{+117}_{-130}	6.0	0.96	$8.00^{+0.95}_{-0.88}$
NGC 4051 (3)	5.5	$1.74^{+0.20}_{-0.13}$	$6.5^{+6.5}_{-4.1}$	189^{+172}_{-189}	3.0	0.98	350^{+254}_{-265}	7.7	0.83	377^{+322}_{-352}	5.3	0.90	$7.71^{+3.07}_{-1.20}$
NGC 4593 (1)	5.4	$1.56^{+0.05}_{-0.03}$	$0.0^{+2.0}_{-0.0}$	59^{+63}_{-58}	3.3	1.06	97^{+81}_{-74}	6.0	0.96	< 140	0.8	1.17	$7.60^{+1.19}_{-1.37}$
NGC 4593 (2)	9.2	$1.72^{+0.05}_{-0.04}$	$0.0^{+1.1}_{-0.0}$	< 130	0.4	1.94	< 140	0.1	1.96	< 102	0.0	1.97	–
MCG-6-30-15 (1)	8.5	$1.63^{+0.05}_{-0.03}$	$3.9^{+2.1}_{-1.3}$	189^{+48}_{-59}	8.9	4.81	330^{+64}_{-77}	26.8	3.08	296^{+70}_{-88}	10.9	4.52	$7.94^{+0.27}_{-0.32}$
MCG-6-30-15 (2)	17.6	$1.84^{+0.02}_{-0.04}$	$1.1^{+0.7}_{-1.1}$	71^{+47}_{-36}	3.9	3.28	146^{+58}_{-53}	9.6	2.70	137^{+62}_{-78}	3.6	3.31	$7.73^{+0.39}_{-0.47}$
MCG-6-30-15 (3)	21.4	$1.79^{+0.02}_{-0.01}$	$0.1^{+0.7}_{-0.1}$	148^{+26}_{-28}	22.1	4.53	242^{+36}_{-33}	70.7	2.18	213^{+46}_{-49}	12.3	5.79	$7.93^{+0.15}_{-0.43}$
IC 4329a	36.7	$1.80^{+0.02}_{-0.02}$	$1.5^{+0.5}_{-0.5}$	66^{+19}_{-17}	6.1	6.72	131^{+26}_{-25}	18.4	4.72	107^{+32}_{-31}	5.6	6.84	$7.95^{+0.23}_{-0.27}$
NGC 5506	27.8	$1.77^{+0.03}_{-0.03}$	$29.5^{+1.4}_{-1.4}$	108^{+31}_{-28}	7.5	5.69	220^{+39}_{-51}	24.1	3.69	177^{+46}_{-59}	6.5	5.90	$7.88^{+0.16}_{-0.20}$
NGC 5548 (1)	10.2	$1.69^{+0.02}_{-0.02}$	$0.0^{+0.6}_{-0.0}$	< 70	0.6	1.87	< 80	0.5	1.88	< 70	0.0	1.92	–
NGC 5548 (2)	4.6	$1.35^{+0.11}_{-0.11}$	$10.4^{+4.8}_{-4.6}$	< 240	2.7	1.13	198^{+159}_{-141}	6.9	0.97	227^{+218}_{-212}	3.9	1.08	$7.90^{+6.57}_{-7.90}$
NGC 5548 (3)	9.4	$1.49^{+0.05}_{-0.04}$	$2.8^{+1.8}_{-1.2}$	98^{+49}_{-59}	7.4	1.43	160^{+63}_{-72}	19.6	1.02	165^{+90}_{-104}	6.6	1.47	$7.91^{+0.53}_{-0.54}$
NGC 5548 (4)	9.9	$1.57^{+0.06}_{-0.04}$	$0.8^{+1.9}_{-0.8}$	113^{+57}_{-64}	13.7	0.85	141^{+67}_{-76}	16.5	0.79	< 190	2.6	1.22	$7.55^{+0.58}_{-0.77}$
NGC 5548 (5)	14.4	$1.69^{+0.04}_{-0.03}$	$0.8^{+1.3}_{-0.8}$	65^{+37}_{-46}	3.2	2.21	113^{+47}_{-53}	10.1	1.75	143^{+66}_{-79}	6.7	1.95	$7.86^{+0.61}_{-0.42}$
NGC 5548 (6)	10.1	$1.66^{+0.02}_{-0.02}$	$0.0^{+0.8}_{-0.0}$	83^{+41}_{-37}	7.9	2.08	133^{+48}_{-45}	20.5	1.48	141^{+70}_{-65}	7.3	2.12	$8.00^{+0.42}_{-0.58}$
NGC 5548 (7)	7.1	$1.61^{+0.04}_{-0.04}$	$0.0^{+1.0}_{-0.0}$	74^{+80}_{-74}	3.0	1.20	120^{+93}_{-87}	6.4	1.06	< 200	1.0	1.30	$8.00^{+1.28}_{-1.53}$
NGC 5548 (8)	12.2	$1.66^{+0.02}_{-0.02}$	$0.0^{+0.5}_{-0.0}$	< 70	0.8	2.01	< 90	1.0	1.99	< 90	0.1	2.07	–
NGC 5548 (9)	4.9	$1.55^{+0.08}_{-0.05}$	$0.4^{+2.8}_{-0.4}$	< 130	0.4	1.24	< 180	1.8	1.17	< 230	0.8	1.22	–
NGC 5548 (10)	4.9	$1.64^{+0.04}_{-0.04}$	$0.0^{+1.1}_{-0.0}$	< 90	0.0	1.89	< 180	1.5	1.77	< 220	0.7	1.83	–
NGC 5548 (11)	6.0	$1.68^{+0.07}_{-0.05}$	$0.0^{+1.5}_{-0.0}$	< 150	0.6	1.34	170^{+124}_{-121}	6.9	1.06	216^{+179}_{-167}	5.5	1.11	$8.29^{+1.50}_{-2.05}$
Mrk 841 (1)	2.0	$1.56^{+0.17}_{-0.13}$	$4.4^{+5.9}_{-4.4}$	< 360	1.7	1.37	368^{+314}_{-291}	5.0	1.21	446^{+414}_{-344}	5.0	1.21	$8.18^{+2.41}_{-1.31}$
Mrk 841 (2)	1.7	$1.57^{+0.18}_{-0.16}$	$0.0^{+6.1}_{-0.0}$	< 240	0.0	0.86	< 320	0.0	0.86	< 640	0.0	0.86	–

Table 6 – *continued*

Name	A[a]	Γ^{b}_{2-18}	N_{H}[c]	N_{HFe}[d]	F[e]	χ^{2f}_{ν}	N_{HFe}[g]	F[h]	χ^{2i}_{ν}	N_{HFe}[j]	F[k]	χ^{2l}_{ν}	E^{m}_{th}
3C 382 (1)	2.7	$1.52^{+0.12}_{-0.10}$	$1.8^{+4.4}_{-1.8}$	< 180	0.2	1.13	< 290	1.4	1.07	< 330	1.0	1.09	–
3C 382 (2)	2.6	$1.53^{+0.09}_{-0.07}$	$0.0^{+3.8}_{-0.0}$	< 130	0.2	0.86	< 240	0.2	0.86	< 490	1.6	0.81	–
3C 382 (3)	2.3	$1.46^{+0.05}_{-0.05}$	$0.0^{+2.0}_{-0.0}$	< 100	0.1	1.10	< 190	0.6	1.08	< 250	0.8	1.07	–
3C 390.3	14.7	$1.80^{+0.01}_{-0.01}$	$0.0^{+0.5}_{-0.0}$	< 30	0.0	2.39	< 40	0.0	2.39	< 40	0.0	2.39	–
Mrk 509 (1)	18.8	$1.85^{+0.02}_{-0.02}$	$0.0^{+0.6}_{-0.0}$	< 40	0.0	5.47	< 50	0.0	5.47	< 70	0.0	5.47	–
Mrk 509 (2)	13.8	$1.73^{+0.03}_{-0.02}$	$0.0^{+0.4}_{-0.0}$	< 60	0.0	3.44	< 40	0.0	3.44	< 30	0.0	3.44	–
Mrk 509 (3)	12.7	$1.77^{+0.02}_{-0.02}$	$0.0^{+0.3}_{-0.0}$	< 40	0.0	2.46	< 70	0.1	2.45	< 40	0.0	2.46	–
Mrk 509 (4)	13.8	$1.74^{+0.02}_{-0.02}$	$0.0^{+0.3}_{-0.0}$	< 20	0.0	1.59	< 40	0.0	1.59	< 40	0.0	1.59	–
H 2106-099 (1)	4.2	$1.84^{+0.06}_{-0.05}$	$0.0^{+1.0}_{-0.0}$	< 50	0.1	1.53	< 70	0.1	1.53	< 80	0.1	1.53	–
H 2106-099 (2)	3.8	$1.88^{+0.09}_{-0.08}$	$0.0^{+2.2}_{-0.0}$	< 190	0.2	0.60	< 300	0.6	0.59	< 370	0.2	0.60	–
NGC 7172	20.3	$1.76^{+0.05}_{-0.04}$	$102.0^{+4.8}_{-3.2}$	56^{+31}_{-36}	5.2	1.76	126^{+41}_{-49}	24.8	1.04	84^{+47}_{-63}	3.1	1.90	$8.00^{+0.42}_{-0.87}$
NGC 7213 (1)	8.5	$1.68^{+0.05}_{-0.04}$	$0.8^{+1.7}_{-0.8}$	< 50	0.0	1.93	< 140	0.5	1.89	< 210	1.9	1.78	–
NGC 7213 (2)	12.2	$1.79^{+0.04}_{-0.03}$	$0.9^{+1.5}_{-0.9}$	< 40	0.0	2.14	133^{+64}_{-70}	7.8	1.59	156^{+83}_{-90}	6.1	1.68	$8.00^{+4.62}_{-0.49}$
NGC 7314	7.0	$1.67^{+0.08}_{-0.08}$	$2.7^{+2.5}_{-2.4}$	105^{+86}_{-83}	5.4	1.03	187^{+115}_{-108}	13.1	0.81	159^{+130}_{-131}	5.2	1.04	$8.00^{+0.78}_{-0.84}$
NGC 7469	11.5	$1.84^{+0.02}_{-0.03}$	$0.0^{+0.8}_{-0.0}$	< 50	0.0	2.90	< 70	0.0	2.90	< 70	0.0	2.90	–
MCG-2-58-22 (1)	3.6	$1.51^{+0.04}_{-0.03}$	$0.0^{+1.4}_{-0.0}$	< 50	0.1	1.52	< 210	2.8	1.36	170^{+128}_{-117}	6.2	1.20	$8.70^{+4.14}_{-5.15}$
MCG-2-58-22 (2)	4.5	$1.51^{+0.14}_{-0.12}$	$2.8^{+4.8}_{-2.8}$	< 210	0.8	1.21	233^{+193}_{-190}	5.2	1.02	282^{+238}_{-233}	5.2	1.02	$10.25^{+2.36}_{-2.93}$
MCG-2-58-22 (3)	3.0	$1.43^{+0.06}_{-0.06}$	$0.0^{+2.6}_{-0.0}$	< 100	0.0	1.20	133^{+147}_{-131}	3.5	1.04	157^{+180}_{-157}	3.3	1.05	$8.72^{+5.01}_{-1.44}$
MCG-2-58-22 (4)	5.0	$1.44^{+0.08}_{-0.05}$	$3.6^{+2.7}_{-2.0}$	80^{+66}_{-72}	3.7	1.15	170^{+91}_{-101}	11.9	0.88	171^{+110}_{-127}	6.3	1.05	$7.90^{+5.27}_{-7.90}$

[a]Power-law flux at 1 keV, 7.1-keV fit, in units of 10^{-3} photon cm^{-2} s^{-1} keV^{-1}. [b]Power-law photon index, 7.1-keV fit. [c]Neutral column density in units of 10^{21} cm^{-2}, 7.1-keV fit. [d]Iron-edge equivalent column density (see text), in units of 10^{21} cm^{-2}, 7.1-keV edge. [e]F-statistic for one additional parameter (N_{HFe}), 7.1-keV edge. [f]For 23 degrees of freedom, 7.1-keV edge. [g]Iron-edge equivalent column density (see text), in units of 10^{21} cm^{-2}, 8.0-keV edge. [h]F-statistic for one additional parameter (N_{HFe}), 8.0-keV edge. [i]For 23 degrees of freedom, 8.0-keV edge. [j]Iron-edge equivalent column density (see text), in units of 10^{21} cm^{-2}, 8.85-keV edge. [k]F-statistic for one additional parameter (N_{NFE}), 8.85-keV edge. [l]For 23 degrees of freedom, 8.85-keV edge. [m]Threshold edge energy, free fit.

8 THE ORIGIN OF THE IRON EMISSION LINE: REPROCESSING IN OPTICALLY THICK GAS

8.1 Transmission models

Transmission of X-rays through neutral or partially ionized gas results in fluorescent line emission. Indeed, the measured X-ray column densities in the heavily obscured sources NGC 4151 and Cen A are sufficient to explain the line emission by fluorescence in a spherical shell. However, the measured soft X-ray absorption column densities along the line of sight to the majority of sources ($N_H \sim 10^{21-22}$ cm^{-2}; see Fig. 4) are insufficient to explain the equivalent widths of the iron line observed in these *Ginga* spectra. Monte Carlo calculations suggest that a line of equivalent width $W_{K\alpha} \sim$ 150 eV, the mean value for our sample, can be produced in a

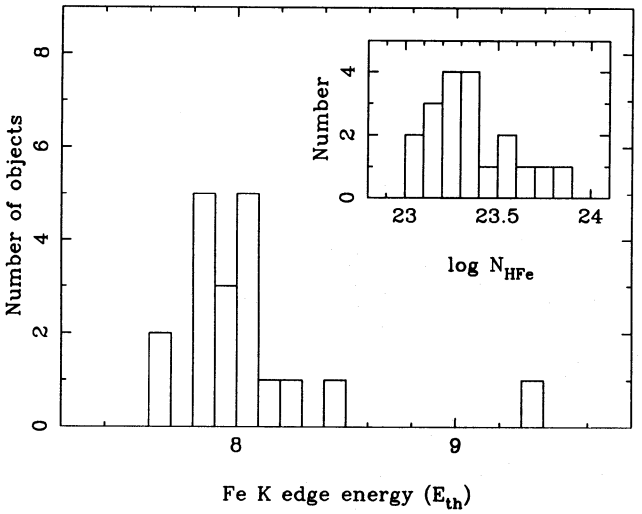

Figure 7. Histogram of the edge energies obtained using power-law plus absorption edge fits. The mean energy $E_{th} = 7.92 \pm 0.12$ keV, higher than the value expected for Fe I (7.1 keV). In fact, this energy suggests an ionization state for the iron of Fe XX. This feature indicates highly ionized material, probably in the line of sight to the X-ray source. The histogram of best-fitting column densities is also shown (inset). Columns are large, of order ~ a few $\times 10^{23}$ cm^{-2}.

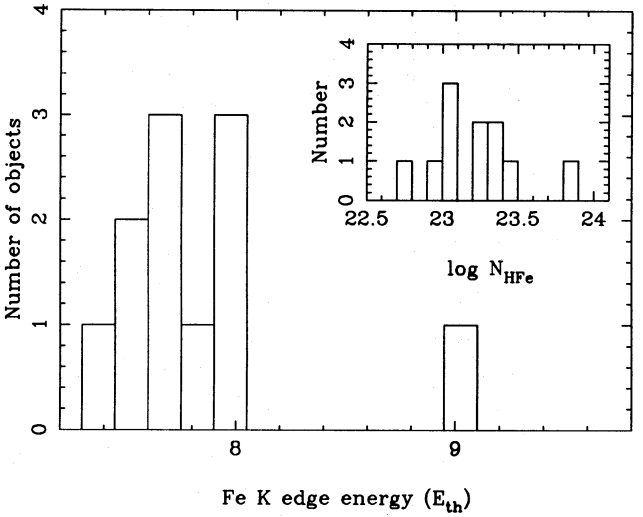

Figure 8. Histogram of the edge energies obtained using power-law plus absorption edge fits *including a narrow emission line at 6.4 keV*. The mean energy is very similar to that where the line is excluded, $E_{th} = 7.8 \pm 0.3$, with no significant intrinsic dispersion ($\sigma_p < 0.82$ at 99 per cent confidence). A component of ionized gas is thus required, even when the line is accounted for. The histogram of best-fitting column densities (inset) indicates that slightly lower columns are required in these fits: $N_{HFe} \sim 10^{23}$ cm^{-2}.

Table 7. Edge fits including a line at 6.4 keV.

Name	A[a]	Γ^b_{2-18}	N_H[c]	$I^d_{K\alpha}$	$W^e_{K\alpha}$	E^f_{th}	N_{HFe}[g]	F[h]	χ^{2i}_ν
NGC 3227 (1)	9.4	$1.66^{+0.07}_{-0.03}$	$0.1^{+1.8}_{-0.1}$	$3.7^{+2.7}_{-2.6}$	87 ± 62	$7.78^{+0.79}_{-0.74}$	106^{+78}_{-85}	3.8	1.24
NGC 3516 (1)	5.8	$1.49^{+0.20}_{-0.14}$	$41.9^{+10.3}_{-7.2}$	$5.1^{+4.8}_{-4.5}$	151 ± 137	$7.88^{+0.63}_{-0.86}$	352^{+188}_{-220}	5.1	1.67
NGC 3516 (2)	5.4	$1.48^{+0.19}_{-0.12}$	$65.1^{+13.3}_{-9.1}$	$5.2^{+4.2}_{-3.9}$	169 ± 131	$7.85^{+0.90}_{-1.26}$	275^{+187}_{-189}	8.2	0.82
NGC 3516 (3)	5.2	$1.47^{+0.21}_{-0.20}$	$55.8^{+15.4}_{-12.6}$	$8.1^{+5.4}_{-6.4}$	265 ± 195	$6.99^{+0.94}_{-1.04}$	254^{+186}_{-186}	12.7	0.46
NGC 4051 (2)	4.5	$1.65^{+0.13}_{-0.07}$	$0.9^{+3.5}_{-0.9}$	$0.5^{+6.0}_{-0.5}$	24 ± 287	$8.00^{+2.84}_{-2.65}$	157^{+146}_{-157}	2.9	0.84
NGC 5506	27.9	$1.79^{+0.05}_{-0.05}$	$28.9^{+1.9}_{-1.8}$	$10.9^{+3.9}_{-3.8}$	113 ± 40	$7.44^{+0.92}_{-0.01}$	119^{+62}_{-60}	7.3	1.84
NGC 5548 (3)	9.6	$1.51^{+0.08}_{-0.06}$	$2.9^{+2.3}_{-1.8}$	$3.8^{+3.8}_{-3.3}$	66 ± 62	$7.51^{+1.44}_{-1.43}$	107^{+90}_{-97}	4.3	0.80
NGC 5548 (4)	10.4	$1.61^{+0.08}_{-0.07}$	$1.2^{+2.4}_{-1.2}$	$5.1^{+4.8}_{-4.3}$	98 ± 86	$7.05^{+1.87}_{-1.85}$	83^{+80}_{-83}	8.2	0.35
NGC 7172	18.4	$1.71^{+0.07}_{-0.05}$	$98.3^{+6.3}_{-5.1}$	$1.5^{+3.5}_{-1.5}$	23 ± 54	$8.00^{+0.55}_{-0.70}$	111^{+62}_{-69}	7.4	1.09
NGC 7314	7.0	$1.68^{+0.12}_{-0.06}$	$2.5^{+3.4}_{-2.5}$	$1.6^{+11.4}_{-1.6}$	51 ± 369	$8.00^{+4.58}_{-3.97}$	144^{+169}_{-144}	2.6	0.84
IC4329a	38.4	$1.83^{+0.03}_{-0.03}$	$2.0^{+0.7}_{-0.7}$	$11.4^{+3.2}_{-3.0}$	89 ± 24	$7.63^{+0.53}_{-0.62}$	50^{+40}_{-34}	4.6	1.43
MCG-5-23-16 (1)	8.2	$1.48^{+0.11}_{-0.11}$	$9.2^{+4.1}_{-3.8}$	$9.3^{+5.1}_{-5.1}$	179 ± 99	$9.06^{+1.50}_{-1.10}$	223^{+193}_{-186}	4.3	1.01
MCG-6-30-15 (1)	8.0	$1.61^{+0.08}_{-0.05}$	$2.3^{+2.8}_{-2.0}$	$6.1^{+3.2}_{-2.9}$	151 ± 75	$7.72^{+0.51}_{-0.51}$	231^{+88}_{-106}	7.9	2.23
MCG-6-30-15 (3)	21.7	$1.81^{+0.04}_{-0.02}$	$0.2^{+0.9}_{-0.2}$	$4.5^{+2.5}_{-2.5}$	59 ± 33	$7.45^{+0.41}_{-0.25}$	185^{+45}_{-56}	40.4	1.03
Mrk 335 (1)	2.7	$1.70^{+0.53}_{-0.29}$	$7.6^{+15.1}_{-7.6}$	$0.1^{+4.6}_{-0.1}$	9 ± 410	$7.61^{+1.45}_{-1.02}$	754^{+979}_{-754}	4.2	0.64

[a]Power-law flux at 1 keV, in units of 10^{-3} photon cm^{-2} s^{-1} keV^{-1}. [b]Power-law photon index. [c]Neutral column density, in units of 10^{21} cm^{-2}. [d]Intensity of the 6.4-keV emission line in units of 10^{-4} photon cm^{-2} s^{-1}. [e]Equivalent width of the 6.4-keV emission-line (eV) edge. [f]Edge threshold energy (keV). [g]Iron-edge equivalent column density (see text), in units of 10^{21} cm^{-2}. [h]*F*-statistic for two additional parameters (N_{HFe}, E_{th}). [i]For 21 degrees of freedom.

neutral, solar abundance, spherical cloud of column density $\sim 2\times10^{23}$ cm^{-2} (we have assumed an input photon spectrum of a power law with index $\Gamma = 1.7$). None of our sample sources shows a soft X-ray cut-off consistent with such a high cold column density.

If the abundances in the line-producing plasma were significantly different from the cosmic abundances assumed, in particular if the abundance of iron relative to the elements producing the soft X-ray absorption (O, Ne, Si etc.) were increased, a higher equivalent width would be produced for the observed soft X-ray column. In most cases, an abundance ~ 10–100 times solar values would be required to fit the data, and so an iron K-absorption edge would be expected at 7.1 keV. It has already been shown in Table 6 that such a neutral edge is not preferred in the majority of these sources. In addition, for the required high value of $N_{\rm HFe}$, iron L-shell absorption would become significant and would again violate the soft X-ray constraint.

Alternatively, with a chemical composition close to cosmic, a highly ionized medium would be largely transparent at soft X-ray energies (2–3 keV) and may lead us to underestimate the line-of-sight column density considerably during the spectral fitting. The substantial flux of ionizing photons from the active nucleus is indeed likely to lead to photoionization of any low-density material in the line of sight. We can see from our edge fits in Tables 6 and 7 that the presence of ionized gas is indicated for some sources. The fact that the warm absorber features are common (Section 9) also suggests that the covering fraction of the warm absorber may be high. However, we can reject the ionized absorbing gas as the *major* source of the line emission on the basis of the line energy. The energy of K-shell fluorescence from Fe XX–XXVI (corresponding to absorption at ~ 8–9 keV) is ~ 6.5–6.7 keV (e.g. Makishima 1986), marginally higher than the observed line-energy. Although this warm absorber cannot provide a full explanation for the observed spectrum, it may contribute to both absorption and emission features. This is considered further in the following section.

If the absorber is cold but non-uniform, which has been suggested to explain the complex low-energy X-ray spectrum of NGC 4151 (e.g. Holt et al. 1980; Yaqoob & Warwick 1991), this could again confuse the measurement of $N_{\rm H}$. If this is the case, soft X-rays 'leak' through the uncovered part of the source and produce a characteristic shape in the soft X-ray regime, which would lead to an underestimate of the true column density in a uniform-absorption fit. A similar model, but with $N_{\rm H} \gg 10^{23}$ cm^{-2}, has been proposed to account for the high-energy tail observed in the X-ray spectra of several Seyferts (Matsuoka et al. 1990; Piro, Matsuoka & Yamauchi 1990). Whilst the hard tail could arise from transmission of X-rays through optically thick material, a more likely explanation is that the hard X-rays are predominantly reflected from such material, unless the covering fraction and column density lie in a small range, and are similar for many Seyferts. This partial-covering model may merely be a crude parametrization of the effects of X-ray reflection from cold material described below, and we consider it no further.

Summarizing, none of the transmission models can alone provide an adequate description of the complex spectrum of all the sources in the *Ginga* sample. This leads to the conclusion that the bulk of the features arise in cool dense material out of the line of sight to the primary source of X-rays.

8.2 Reflection models

Guilbert & Rees (1988) first suggested that optically thick material might imprint features on the X-ray spectra of AGN. Subsequently, Lightman & White (1988) calculated the expected continuum reflected from material with $\tau_{\rm T} \gg 1$. These workers found that a broad 'hump' of emission peaking at ~ 30–50 keV would be expected, due to the competition between bound–free absorption and Compton scattering in the reflecting medium. The material producing the UV/soft X-ray 'bump' may well be optically thick, and is a likely source for the iron fluorescence.

Detailed Monte Carlo calculations of the line and continuum from a reflective slab lying behind a power-law source of X-rays have now been carried out (George & Fabian 1991, hereafter GF; Matt et al. 1991). For further details of these calculations, the reader is referred to GF, whose results are used here. Initially, a reflecting slab is assumed to lie behind a source isotropically emitting a power-law X-ray spectrum up to 1 MeV. Photons are injected from this source into the reflecting medium and are followed until they either re-emerge after Compton scattering or fluorescence, or are absorbed. Both iron Kα (~ 6.4 keV) and Kβ (~ 7.1 keV) emissions are computed, along with nickel Kα (~ 7.5 keV). The only line-broadening process included is Compton scattering (which dominates over, e.g., thermal broadening), but this is not significant when compared to the resolution of the LAC. The line equivalent width is a function of the inclination, i, of the observer relative to the normal to the slab, due to the increased path-length through the absorbing medium for photons escaping at grazing angles (as $i \rightarrow 90°$; edge on).

For typical spectral indices measured here, the maximum equivalent width, attained for a face-on geometry ($i \sim 0°$), is of order ~ 150 eV. There is also an iron K-edge in the reflected spectrum, but the iron Kβ line (7.1 keV) serves to fill in this absorption feature somewhat, which in any case has low contrast when added into the direct continuum. The edge column density is of order $N_{\rm HFe} \sim 10^{24}$ cm^{-2} in the reflected spectrum, but when added to the direct continuum the effective column density is only $N_{\rm HFe} \sim 4\times10^{22}$ cm^{-2} for the face-on geometry.

The reflected continuum has a characteristic shape in the X-ray band (GF), the primary point being that the reflected spectrum is much flatter than the input power law in the 2–18 keV range of the *Ginga* data. The depletion below ~ 15 keV occurs because of photoelectric absorption in the slab. Above this energy little absorption occurs, and the effective albedo reaches a peak at ~ 30 keV, due to Compton down-scattering of higher energy photons. Finally, the spectrum begins to turn over at energies higher than this, as the scattering cross-section reduces in the Klein–Nishina regime. For the energy band considered here (2–18 keV) the effect of the reflected continuum is then to flatten the observed power, compared to the intrinsic slope, introducing a hard tail above ~ 10 keV.

The overall appearance of the reflected spectrum makes it an attractive interpretation for the observed spectral

features. Not only does a face-on slab introduce an iron line of order 150 eV, as observed, but the reflected continuum provides a natural description for the hard tail above 10 keV seen in the *Ginga* data. The reflected spectrum also contains an iron K-edge, at 7.1 keV. However, as noted above, the effective column density is small, and therefore the observed absorption feature (Section 7) cannot be fully explained by the reflection model. See below for further discussion of this point.

The strengths of the reflection component and iron line depend on many factors, particularly the inclination of the slab or disc, and the solid angle it subtends at the X-ray source. However, because the *shape* of the reflected continuum is a very weak function of the inclination and geometry (GF), we fitted a face-on ($i=0°$) reflection spectrum to the data, but allowed the normalization, $A_{\rm ref}$, to vary. $A_{\rm ref}=1$ corresponds to the reflected component expected from a face-on slab, subtending solid angle 2π at the continuum source, for a power-law illumination with unit normalization. We therefore define our reflection model as

$$F_{\rm x}(E)=[AE^{-\Gamma}+A_{\rm ref}\psi(E,\Gamma)]$$
$$\times\exp(-\sigma_{\rm ph}N_{\rm H})\quad\text{photon cm}^{-2}\,\text{s}^{-1}\,\text{keV}^{-1},\qquad(6)$$

where $\psi(E,\Gamma)$ is the reflected flux for a face-on slab subtending solid angle 2π at the X-ray source illuminated by a power law with $A=1$, and $A_{\rm ref}$ is the reflected normalization.

This normalization embodies the unknowns concerning the inclination and solid angle of the slab, and also allows for variability of the reflection component with respect to the direct continuum, and possible anisotropy or obscuration of this continuum. By examining the ratio $R=A_{\rm ref}/A$ we can then make inferences about these parameters. The results of fits to the *Ginga* data using this slab reflection model including the emission line are shown in Table 8. This model is only formally correct if the reflecting material lies sufficiently far from the putative black hole, so that there is no significant line broadening due to orbital motions and gravitational shifts. However, the expected broadening for a face-on accretion disc is only $\sigma_{\rm K\alpha}\sim 0.4$ keV (Matt et al. 1992), which is comparable to the resolution of the *Ginga* LAC. This approximation should therefore not introduce substantial errors. Notwithstanding the assumption of a non-relativistic reprocessor, these models generally give a better fit than the power-law plus line model, with the same number of free parameters. Statistically acceptable fits ($\chi^2_\nu<1.4$) are obtained for 50/60 spectra (cf. 41 in the case of the power-law plus line fits – see Section 10 for a full discussion of the significance of the reflected continuum). The weighted mean of the normalization ratio, $\overline{R}$, is 0.72 ± 0.05, with a likelihood value of $\langle R\rangle=0.77^{+0.18}_{-0.12}$ and no significant spread ($\sigma_{\rm p}<0.82$ at 90 per cent confidence). Note that these values were derived assuming a solar abundance medium (cf. Section 10). They suggest that, on average, the reprocessing material subtends ~ 1–2π sr at the X-ray source.

9 THE ORIGIN OF THE IRON EDGE: THE WARM ABSORBER

Whilst reflection from cold material provides an excellent explanation for the iron line and 'hard tail' observed in our *Ginga* observations, it cannot account for the deep iron edge observed in some sources. Additionally, even with the reflec-

Table 8. Face-on Compton reflection model. All fits are in the 2–18 keV range.

Name	A[a]	$\Gamma_{\rm int}$[b]	$N_{\rm H}$[c]	$A_{\rm ref}$[d]	χ^2_ν[e]
Mrk 335 (1)	6.3	$2.30^{+0.16}_{-0.44}$	$19.5^{+12.1}_{-9.5}$	$9.4^{+11.1}_{-9.4}$	0.85
Mrk 335 (2)	10.6	$2.20^{+0.28}_{-0.08}$	$0.4^{+4.8}_{-0.4}$	$6.2^{+14.9}_{-6.2}$	0.28
Mrk 335 (3)	7.0	$2.38^{+0.10}_{-0.26}$	$0.0^{+5.3}_{-0.0}$	$9.1^{+12.0}_{-9.1}$	0.93
Mrk 335 (4)	6.7	$2.30^{+0.15}_{-0.45}$	$3.6^{+16.0}_{-3.6}$	$22.2^{+19.2}_{-22.0}$	0.91
NGC 526A	1.8	$1.49^{+0.24}_{-0.19}$	$11.7^{+7.3}_{-6.6}$	$3.8^{+2.3}_{-2.3}$	0.64
Fairall-9	11.5	$1.94^{+0.11}_{-0.08}$	$1.0^{+2.0}_{-1.0}$	$6.2^{+8.1}_{-4.1}$	1.43
3C 111	10.9	$1.77^{+0.07}_{-0.04}$	$18.4^{+2.1}_{-1.9}$	$0.0^{+2.9}_{-0.0}$	1.40
Akn 120	12.3	$1.93^{+0.15}_{-0.07}$	$0.0^{+2.5}_{-0.0}$	$11.6^{+14.1}_{-6.7}$	1.02
NGC 2110	11.5	$1.83^{+0.10}_{-0.09}$	$26.1^{+2.7}_{-2.4}$	$9.1^{+6.0}_{-4.2}$	1.07
NGC 2992	8.1	$2.19^{+0.02}_{-0.19}$	$22.5^{+3.6}_{-4.3}$	$30.7^{+12.0}_{-13.5}$	1.70
NGC 3227 (1)	12.9	$1.89^{+0.07}_{-0.06}$	$4.1^{+1.4}_{-1.3}$	$11.3^{+5.6}_{-4.0}$	1.12
NGC 3227 (2)	11.8	$1.86^{+0.08}_{-0.07}$	$6.3^{+1.6}_{-1.6}$	$12.4^{+5.8}_{-4.4}$	0.82
MCG-5-23-16 (1)	12.6	$1.78^{+0.15}_{-0.09}$	$15.5^{+3.8}_{-2.6}$	$13.8^{+14.9}_{-5.8}$	1.79
MCG-5-23-16 (2)	4.5	$1.59^{+0.23}_{-0.18}$	$16.8^{+6.9}_{-6.3}$	$9.4^{+5.6}_{-4.2}$	0.85
NGC 3516 (1)	14.6	$2.13^{+0.18}_{-0.13}$	$56.7^{+8.0}_{-5.5}$	$32.3^{+28.9}_{-12.3}$	1.57
NGC 3516 (2)	12.3	$2.04^{+0.15}_{-0.13}$	$80.0^{+9.2}_{-7.6}$	$23.7^{+14.8}_{-10.5}$	0.84
NGC 3516 (3)	11.8	$2.06^{+0.23}_{-0.17}$	$69.2^{+12.9}_{-9.5}$	$27.1^{+34.2}_{-14.4}$	0.62
NGC 3783	25.7	$2.00^{+0.04}_{-0.08}$	$26.3^{+1.1}_{-1.6}$	$30.3^{+6.4}_{-12.2}$	4.11
NGC 4051 (1)	4.1	$1.75^{+0.22}_{-0.09}$	$1.2^{+4.7}_{-1.2}$	$3.6^{+6.4}_{-3.1}$	1.12
NGC 4051 (2)	6.0	$1.86^{+0.13}_{-0.09}$	$4.7^{+2.8}_{-2.0}$	$3.6^{+5.4}_{-2.4}$	0.82
NGC 4051 (3)	8.1	$2.00^{+0.34}_{-0.20}$	$11.6^{+7.1}_{-4.7}$	$5.1^{+21.5}_{-5.1}$	1.02
NGC 4593 (1)	6.8	$1.74^{+0.10}_{-0.09}$	$2.5^{+2.3}_{-2.1}$	$4.7^{+3.6}_{-2.4}$	0.58
NGC 4593 (2)	10.8	$1.89^{+0.12}_{-0.07}$	$0.0^{+2.5}_{-0.0}$	$12.5^{+10.5}_{-5.6}$	0.91
MCG-6-30-15 (1)	14.4	$2.03^{+0.10}_{-0.05}$	$10.0^{+2.3}_{-1.7}$	$23.5^{+12.0}_{-6.1}$	3.34
MCG-6-30-15 (2)	23.8	$2.07^{+0.07}_{-0.04}$	$4.6^{+1.4}_{-0.9}$	$22.3^{+13.4}_{-5.2}$	0.99
MCG-6-30-15 (3)	30.7	$2.06^{+0.04}_{-0.04}$	$4.6^{+0.8}_{-0.8}$	$25.3^{+6.5}_{-6.1}$	4.38
IC 4329a	48.1	$2.00^{+0.02}_{-0.03}$	$4.8^{+0.5}_{-0.5}$	$37.0^{+6.1}_{-7.4}$	1.16
NGC 5506	42.0	$2.08^{+0.06}_{-0.04}$	$34.8^{+1.7}_{-1.2}$	$46.7^{+14.9}_{-8.4}$	1.14
NGC 5548 (1)	11.0	$1.77^{+0.05}_{-0.03}$	$0.0^{+1.1}_{-0.0}$	$5.8^{+2.8}_{-2.4}$	0.87
NGC 5548 (2)	6.7	$1.65^{+0.23}_{-0.16}$	$14.7^{+6.0}_{-5.0}$	$9.1^{+10.2}_{-4.6}$	0.68
NGC 5548 (3)	11.7	$1.66^{+0.09}_{-0.05}$	$5.6^{+2.1}_{-1.3}$	$6.0^{+4.7}_{-2.5}$	1.21
NGC 5548 (4)	13.4	$1.79^{+0.10}_{-0.07}$	$4.5^{+2.2}_{-1.7}$	$8.9^{+7.4}_{-4.3}$	0.57
NGC 5548 (5)	18.2	$1.86^{+0.07}_{-0.05}$	$3.6^{+1.5}_{-1.0}$	$10.3^{+7.5}_{-3.9}$	1.31
NGC 5548 (6)	12.8	$1.84^{+0.06}_{-0.06}$	$2.7^{+1.3}_{-1.3}$	$7.9^{+4.0}_{-3.2}$	1.52
NGC 5548 (7)	9.4	$1.84^{+0.12}_{-0.12}$	$2.8^{+2.6}_{-2.5}$	$9.1^{+8.4}_{-5.0}$	0.62
NGC 5548 (8)	13.2	$1.75^{+0.05}_{-0.04}$	$0.0^{+1.3}_{-0.0}$	$6.3^{+3.3}_{-2.9}$	1.28
NGC 5548 (9)	6.4	$1.74^{+0.14}_{-0.12}$	$3.3^{+3.1}_{-3.1}$	$4.9^{+5.4}_{-3.2}$	0.88
NGC 5548 (10)	5.7	$1.80^{+0.11}_{-0.06}$	$0.0^{+2.2}_{-0.0}$	$5.8^{+4.5}_{-2.4}$	0.79
NGC 5548 (11)	7.5	$1.87^{+0.19}_{-0.13}$	$1.9^{+3.8}_{-1.9}$	$6.8^{+11.6}_{-4.6}$	0.96
Mrk 841 (1)	5.1	$2.30^{+0.30}_{-0.28}$	$13.9^{+6.0}_{-4.4}$	$22.9^{+7.3}_{-16.3}$	0.69
Mrk 841 (2)	2.0	$1.77^{+0.68}_{-0.31}$	$0.0^{+9.8}_{-0.0}$	$2.8^{+22.2}_{-2.8}$	0.79
3C 382 (1)	4.8	$1.98^{+0.23}_{-0.34}$	$8.1^{+4.5}_{-6.3}$	$10.9^{+9.0}_{-8.8}$	0.65
3C 382 (2)	3.4	$1.77^{+0.39}_{-0.20}$	$1.9^{+6.9}_{-0.0}$	$4.5^{+15.0}_{-3.5}$	0.61
3C 382 (3)	2.8	$1.66^{+0.15}_{-0.11}$	$0.0^{+3.8}_{-0.0}$	$4.0^{+2.7}_{-1.9}$	0.41
3C 390.3	15.6	$1.86^{+0.03}_{-0.02}$	$0.0^{+0.8}_{-0.0}$	$6.3^{+3.0}_{-2.4}$	1.23
Mrk 509 (1)	21.5	$1.99^{+0.05}_{-0.03}$	$0.0^{+0.2}_{-0.0}$	$23.6^{+9.3}_{-6.3}$	1.93
Mrk 509 (2)	15.5	$1.85^{+0.05}_{-0.04}$	$0.0^{+0.3}_{-0.0}$	$11.7^{+5.4}_{-4.1}$	1.92
Mrk 509 (3)	13.9	$1.87^{+0.04}_{-0.03}$	$0.0^{+0.6}_{-0.0}$	$9.1^{+3.8}_{-3.0}$	0.73
Mrk 509 (4)	14.7	$1.80^{+0.04}_{-0.02}$	$0.0^{+0.6}_{-0.0}$	$6.0^{+3.9}_{-3.7}$	1.16
H 2106-099 (1)	4.7	$1.95^{+0.13}_{-0.10}$	$0.0^{+2.0}_{-0.0}$	$3.7^{+5.5}_{-3.1}$	1.30
H 2106-099 (2)	4.3	$2.02^{+0.38}_{-0.14}$	$0.0^{+6.9}_{-0.0}$	$4.9^{+14.9}_{-4.2}$	0.40
NGC 7172	23.7	$1.87^{+0.06}_{-0.04}$	$103.3^{+4.8}_{-3.4}$	$8.7^{+6.0}_{-3.8}$	1.32
NGC 7213 (1)	10.1	$1.82^{+0.11}_{-0.10}$	$2.8^{+2.3}_{-2.2}$	$6.4^{+5.7}_{-4.0}$	1.49
NGC 7213 (2)	14.4	$1.92^{+0.09}_{-0.06}$	$2.9^{+1.9}_{-1.3}$	$7.7^{+8.1}_{-4.0}$	1.51
NGC 7314	9.6	$1.91^{+0.11}_{-0.11}$	$6.6^{+2.5}_{-2.7}$	$7.5^{+7.7}_{-4.6}$	0.81
NGC 7469	13.1	$1.97^{+0.06}_{-0.04}$	$0.0^{+1.3}_{-0.0}$	$13.8^{+7.5}_{-4.9}$	1.14
MCG-2-58-22 (1)	4.0	$1.61^{+0.13}_{-0.07}$	$0.1^{+3.1}_{-0.0}$	$3.1^{+2.3}_{-2.0}$	1.15
MCG-2-58-22 (2)	6.1	$1.72^{+0.24}_{-0.16}$	$5.9^{+5.7}_{-4.2}$	$4.9^{+11.0}_{-3.9}$	1.02
MCG-2-58-22 (3)	3.6	$1.59^{+0.17}_{-0.07}$	$0.6^{+3.8}_{-0.0}$	$4.5^{+5.2}_{-2.6}$	0.71
MCG-2-58-22 (4)	6.4	$1.62^{+0.11}_{-0.08}$	$6.1^{+2.8}_{-2.2}$	$4.6^{+2.8}_{-2.3}$	0.80

[a]Power-law flux at 1 keV in units of 10^{-3} photon cm^{-2} s^{-1} keV^{-1}. [b]Underlying power-law photon index. [c]Neutral column density in units of 10^{21} cm^{-2}. [d]Normalization of reflected component (see text). [e]For 23 degrees of freedom.

tion model, some observations still give unacceptable χ^2. Examination of the data–model residuals generally shows this to be a poor fit to the observed absorption profile at 2–4 keV, which is not well matched to the Morrison & McCammon opacities. This, as stated in the introduction, we explain by the fact that a substantial fraction of sources suffer absorption by *highly ionized* gas in the line of sight to the nucleus, the so-called warm absorber. Here we attempt to assess the significance, and quantify the parameters, of the warm gas. As a first test, we have repeated our fits with an iron absorption edge, but this time with the reflection component of GF included. Using the *F*-test, we find a significant improvement (at >90 per cent confidence) when an edge is included for NGC 4051 (one observation), NGC 5548 (four observations), MCG-2-58-22 (two observations), MCG-5-23-16 (one observation), MCG-6-30-15 (two observations) and Mrk 335 (one observation). This model is necessarily rather complex, and the values of the edge energy are not well constrained. However, they generally lie between 8 and 9 keV, and the equivalent column densities are of order $N_{\rm HFe} \sim 10^{23}$ cm^{-2}, as found in the simpler fits (Section 7).

A more promising prospect for measuring the parameters of the ionized gas is to fit a full warm absorber model, as the imprints of S, Ar, Si and so on may be left on the 2–5 keV spectrum, giving additional constraints. As shown in Section 5, around ~ 50 per cent of our sources require additional absorption at soft X-ray energies over that expected from H I in our own Galaxy, as found, for example with *EXOSAT* (Turner & Pounds 1989). We do not know a priori whether this arises from photoionized material, or cold gas, for example in the host galaxy (but see the discussion of the *ROSAT* measurements below). We have tested this by introducing the ionization parameter as an additional free parameter in the power-law plus reflection fits, rather than by assuming a cold $N_{\rm H}$. We define the dimensionless ionization parameter, U, by

$$U = Q/4\pi n_{\rm e} r^2 c, \qquad (7)$$

where Q is the flux of ionizing photons in photon s^{-1}, $n_{\rm e}$ is the electron density, and r is the distance of the absorbing gas from the ionizing source. We define the equivalent hydrogen column density of the warm gas as $N_{\rm H}^{*} = n_{\rm e} l$, where l is the radial thickness of the absorbing medium. We have used the photoionization code of Yaqoob & Warwick (1991) to compute the absorption profile expected from the ionized gas. The ionizing continuum is assumed to be a power law, but with free normalization and index as defined in the fit. The remainder of the continuum is the same as that given by Matthews & Ferland (1987) and joins smoothly to the ionizing flux. The temperature of the ionized gas is calculated in the code, assuming a balance between heating and cooling. The cold columns due to our Galaxy, which are of order a few $\times 10^{20}$ cm^{-2} and therefore negligible in the fits, have been ignored.

These fits show a significant improvement in χ^2 (at >90 per cent confidence) for the following objects (number of observations in brackets): Mrk 335 (1), NGC 2110, NGC 2992, NGC 3227 (2), NGC 3783, 3C 382 (1), NGC 4051 (1), NGC 5548 (8), NGC 7213 (2), IC 4329a, MCG-5-23-16 (2), MCG-6-30-15 (2) and MCG-2-58-22 (4). These represent ~ 50 per cent of the sample. The parameters for these fits are detailed in Table 9. Unsurprisingly, all objects in which a significant iron edge was detected in the fits including reflection are included in this list, but there are several additional objects, demonstrating the need to account for all elements when assessing the significance of the warm absorber.

We have plotted the histograms of U and $N_{\rm H}^{*}$ in Fig. 9 and find mean values $\overline{\log U} = 0.13 \pm 0.04$ and $\overline{\log N_{\rm H}} = 22.84 \pm 0.04$. Note that these values do not allow for any intrinsic spread in these quantities (cf. equation 5). The mean value of the ionization parameter is two orders of magnitude higher than that typically found for standard BLR models, and the equivalent hydrogen column density is at least an order of magnitude higher than the typical apparent 'cold' absorption columns (Section 5) in these sources.

10 STRENGTH OF THE REFLECTED CONTINUUM AND THE IRON ABUNDANCE

As stated in Section 4, the hard tail observed in the *Ginga* spectra indicates an additional component. Such a feature would naturally arise if the primary X-rays were reflected from optically thick material, as shown in Section 8. Indeed, the fact that fits to the solar abundance reflection model of GF are better than simple power-law plus line fits suggests that the reflection component is generally required.

If the bulk of the line does indeed arise from fluorescence in optically thick material, a broad anticorrelation would be expected between Γ and the observed equivalent width. This arises because the reflected continuum is flatter than the direct power law. For larger equivalent widths the proportion of the accompanying reflected continuum should be greater, which will flatten the *apparent* power-law continuum in a simple fit. Fig. 10 shows the relationship between Γ, derived from a simple power-law fit, and the equivalent width from the power-law plus line fits. A Spearman rank correlation indicates a significant trend at >99 per cent confidence and a linear correlation is significant at >98 per cent confidence. The data are compatible with the theoretical prediction of the slab reflection model (GF), shown by the solid lines in Fig. 10. These model predictions, as well as the fits including the reflected continuum, indicate a steeper intrinsic power law than that found for the simple power-law fits, in the range $\Gamma_{\rm int} = 1.8$–2.0. This has profound implications for AGN spectral modelling (see Section 11). The correlation also shows that the underlying spectral index lies in a relatively narrow range.

We have also performed additional fits to quantify the significance of the reflected continuum for each source. An additional benefit of these fits is that they can be used to give a crude measure of the iron abundance. Whilst the strength of the iron emission line is a strong function of the iron abundance, the reflected continuum depends little on this parameter (GF; Matt et al. 1991). The continuum spectra generated by the Monte Carlo technique have therefore been tested against the data, to see whether this model can provide a good fit to the hard tail. An arbitrary face-on inclination was again chosen for the slab. The fit was performed with a narrow ($\sigma_{\rm K\alpha}$) Gaussian line, fixed at 6.4 keV, in addition to the reflected continuum component. Clearly, this is an extremely complex model and the constraints on the parameters are generally poor, but we find that the inclusion of the reflected component as an additional free parameter

Table 9. Warm absorber model, including Compton reflection. Note that, in some cases, the parameters cannot be constrained, as the detection of the warm absorber is of low significance. In these cases the exact confidence limits have been omitted. In some cases it is impossible to determine the upper limit on the column density of the warm absorber because the material then becomes optically thick.

Name	A[a]	Γ^{b}_{int}	$\log N_H{}^{*c}$	$\log U^{d}$	A^{e}_{ref}	F[f]	χ^2_ν[g]
Mrk 335 (a)	36.6	3.1 (> 2.1)	23.3 (> 23.6)	0.9 (> 0.0)	58.0 (> 5.0)	13.5	0.55
NGC 2110	15.2	$1.93^{+0.12}_{-0.09}$	$22.6^{+0.3}_{-0.2}$	-0.4 (< 0.4)	11^{+9}_{-6}	11.7	0.73
NGC 2992	11.1	$2.30^{+0.22}_{-0.20}$	$22.8^{+0.3}_{-0.5}$	0.1 (< 0.4)	37^{+33}_{-19}	4.1	1.50
NGC 3227 (1)	14.8	$1.96^{+0.09}_{-0.09}$	$22.2^{+0.4}_{-0.7}$	-0.1 (< 0.1)	12^{+7}_{-5}	5.3	0.94
NGC 3227 (2)	14.5	$1.93^{+0.10}_{-0.09}$	$22.6^{+0.2}_{-0.7}$	$-0.03^{+0.15}_{-2.0}$	13^{+7}_{-7}	9.5	0.60
MCG-5-23-16 (1)	19.1	$1.91^{+0.15}_{-0.11}$	$22.9^{+0.2}_{-0.2}$	$0.02^{+0.16}_{-0.19}$	15^{+18}_{-9}	23.9	0.90
MCG-5-23-16 (2)	8.2	$1.57^{+0.44}_{-0.19}$	$23.6^{+0.2}_{-1.3}$	$0.2^{+0.2}_{-1.2}$	3^{+23}_{-3}	8.2	0.65
NGC 3783	38.4	$2.11^{+0.06}_{-0.08}$	$22.96^{+0.07}_{-0.09}$	$0.1^{+0.1}_{-0.1}$	24^{+13}_{-11}	86.7	0.87
NGC 4051 (3)	11.7	$2.13^{+0.45}_{-0.23}$	$22.8^{+0.4}_{-0.5}$	$0.1^{+0.4}_{-0.8}$	4^{+42}_{-4}	7.8	0.79
MCG-6-30-15 (1)	17.6	$2.10^{+0.09}_{-0.14}$	$22.91^{+0.07}_{-0.06}$	$0.16^{+0.09}_{-0.04}$	16^{+2}_{-7}	13.5	2.16
MCG-6-30-15 (3)		$2.18^{+0.06}_{-0.06}$	$22.56^{+0.11}_{-0.14}$	$0.19^{+0.06}_{-0.10}$	31^{+9}_{-9}	32.2	1.86
IC 4329a	48.1	$2.03^{+0.04}_{-0.03}$	$22.0^{+0.2}_{-0.3}$	$-0.4^{+0.3}_{-1.6}$	34^{+9}_{-8}	5.3	0.98
NGC 5548 (2)	10.5	$1.82^{+0.23}_{-0.24}$	$22.9^{+0.3}_{-0.8}$	-0.1 (< 0.2)	11^{+17}_{-9}	7.3	0 54
NGC 5548 (3)	15.7	$1.79^{+0.10}_{-0.10}$	$22.70^{+0.14}_{-0.35}$	$-0.07^{+}_{-0.27}$	7^{+6}_{-5}	25.1	0.59
NGC 5548 (4)	12.5	$1.86^{+0.12}_{-0.12}$	$22.5^{+0.3}_{-1.0}$	-0.06 (< 0.12)	9^{+8}_{-5}	5.8	0.48
NGC 5548 (5)	21.2	$1.96^{+0.08}_{-0.07}$	$22.5^{+0.3}_{-0.4}$	$0.05^{+0.11}_{-0.08}$	13^{+7}_{-6}	26.4	0.62
NGC 5548 (6)	14.4	$1.89^{+0.09}_{-0.07}$	$22.2^{+0.3}_{-0.8}$	-0.11 (< 0.03)	8^{+6}_{-4}	3.8	1.35
NGC 5548 (8)	15.1	$1.77^{+0.06}_{-0.06}$	23.2	0.7	6^{+4}_{-3}	4.1	1.12
NGC 5548 (10)	8.3	$1.81^{+0.16}_{-0.08}$	23.6 (> 22.0)	$0.9^{+1.0}_{-0.9}$	6^{+5}_{-5}	10.4	0.56
NGC 5548 (11)	9.8	$1.88^{+0.13}_{-0.17}$	23.3 (> 22.3)	0.7	6^{+7}_{-6}	4.7	0.83
3C 382 (2)	5.0	$1.90^{+0.40}_{-0.40}$	22.9	0.2	5^{+20}_{-5}	3.7	0.55
NGC 7213 (1)	13.3	$1.88^{+0.14}_{-0.12}$	$22.9^{+0.3}_{-0.5}$	$0.2^{+0.3}_{-0.3}$	5^{+8}_{-5}	5.8	1.23
NGC 7213 (2)	17.7	$2.01^{+0.11}_{-0.11}$	$22.5^{+0.3}_{-0.8}$	$0.1^{+0.6}_{-1.0}$	9^{+10}_{-9}	7.0	1.20
MCG-2-58-22 (1)	6.0	$1.60^{+0.14}_{-0.09}$	23.7 (> 22.6)	$0.7^{+0.9}_{-0.7}$	2^{+7}_{-2}	7.7	0.89
MCG-2-58-22 (2)	9.3	$1.84^{+0.16}_{-0.29}$	23.0 (> 22.0)	$0.1^{+0.6}_{-0.9}$	4^{+13}_{-4}	6.9	0.81
MCG-2-58-22 (3)	5.5	$1.59^{+0.21}_{-0.14}$	23.7 (> 21.3)	0.7	3^{+6}_{-3}	4.9	0.61
MCG-2-58-22 (4)	9.3	$1.74^{+0.13}_{-0.14}$	$22.9^{+0.2}_{-0.4}$	-0.04	4^{+5}_{-4}	41.5	0.29

[a]Power-law flux at 1 keV in units of 10^{-3} photon cm^{-2} s^{-1} keV^{-1}. [b]Underlying power-law photon index. [c]Equivalent hydrogen column density of ionized material in units of cm^{-2}. [d]Ionization parameter (see text). [e]Normalization of reflected component (see text). [f]*F*-statistic for the addition of one extra parameter. [g]For 22 degrees of freedom.

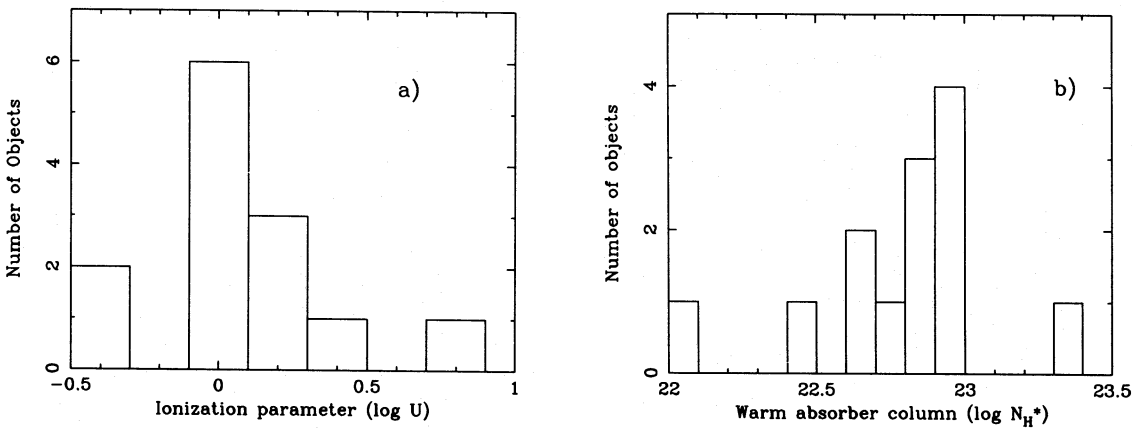

Figure 9. Histograms of the (a) ionization parameters and (b) column densities of the warm absorber, for the sources in which it is significantly detected. As was found for the edge fits, the columns are typically 10^{23} cm^{-2}. The ionization parameter is very high compared, for example, to the broad-line clouds (~ 2 orders of magnitude higher). The very high degree of ionization means that the warm absorber is very difficult to detect in other wavebands (e.g. from its line emission).

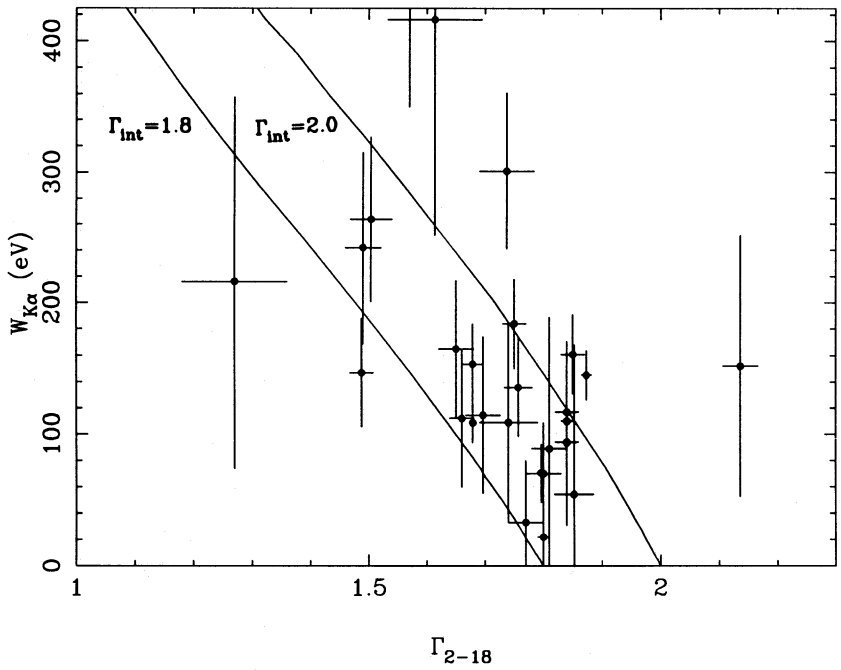

Figure 10. 6.4-keV equivalent width derived from a power-law plus line fit versus the 'apparent' photon index Γ, derived from a simple power-law fit. A Spearman correlation indicates a trend (anticorrelation) at >99 per cent confidence. The solid lines show the Monte Carlo predictions for two underlying photon indices ($\Gamma_{int}=1.8$ and $\Gamma_{int}=2.0$), clearly compatible with the bulk of the data, as long as the intrinsic index is high ($\Gamma_{int}=1.8$–2.0).

improved the fit significantly for 34/60 spectra (17 objects). The Compton reflection component is therefore an excellent fit to the 'hard tail' described previously.

Because of the poor constraints, no significant correlation between the equivalent width and strength of the reflected continuum has been established. However, we can define the *mean* properties of the sample. Using equation (5), we find a mean equivalent width in these fits of 114 ± 18 eV with *no significant dispersion* ($\sigma_p<67$ eV at 90 per cent confidence). The mean normalization ratio for the reflected continuum is $\langle R\rangle=0.53\pm0.28$, relative to a face-on slab. This value is slightly lower than, but consistent with, the value of R derived from the reflection model including the iron emission line at solar abundance (Section 8). *Assuming* a constant value for these parameters we find $\overline{W_{K\alpha}}=112\pm8$ eV and $\overline{R}=0.52\pm0.18$. These values fit in very well with the idea that an accretion disc produces the iron line and reflection hump in AGN. For an *intrinsic* photon spectral index of 1.9, the maximum equivalent width (i.e. for a face-on slab), assuming solar abundances, is ~150 eV, and the value of $R\equiv1$. However, unless there are substantial selection effects, we would expect to observe the accretion disc at all inclination angles. We would therefore predict the *mean* parameters for a sample of accretion discs to be similar to that for an accretion disc inclined at 60°, the typical viewing angle, which is ~70 per cent of the face-on value (Matt et al. 1992). This agrees rather well with our values. The parameters also indicate that the iron abundance in these objects is roughly equal to the solar value. We find $A_{Fe}=1.4\pm0.6$ on the basis of our mean values, consistent with cosmic abundance. These values also imply that the X-ray emission in these objects is not strongly isotropic.

10.1 The underlying X-ray continuum

As we have seen, the 2–20 keV spectra of Seyfert galaxies are not well approximated by a power law, as was previously thought. This means that the estimates of the spectral index of the underlying continuum with *HEAO-1* and *EXOSAT* were not correct. In particular, both the reflected continuum component and the warm absorption produce an apparent flattening of the continuum in our energy range. To estimate the mean photon index of the intrinsic X-ray continuum in Seyferts, we have used the more complex models described in Sections 8 and 9. In Fig. 11, we show the histogram of spectral indices obtained from either power-law plus reflection fits (Table 8) or power-law, reflection plus warm absorber fits (Table 9). The warm absorber has only been included in cases where there is a significant improvement in the fit. The mean value of the *intrinsic* spectral index is found to be $\Gamma_{int}=1.95\pm0.05$, with a significant dispersion of $\sigma_p=0.15\pm0.04$. The fact that the underlying power-law index is close to $\Gamma=2$ has important consequences for theoretical models, and this is addressed further in Section 11. In addition, although the values in Fig. 11 are concentrated around the mean, there *are* real deviations in the index from source to source, even when the reflection and warm absorber (which have the ability to alter the simple power-law index substantially and therefore introduce an apparent spread) are accounted for.

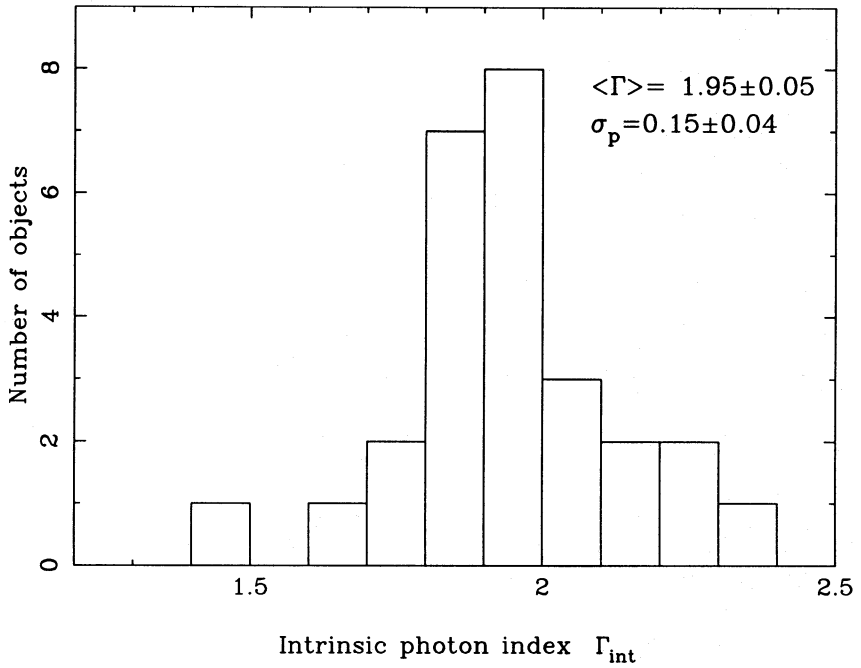

Figure 11. Histogram of intrinsic photon indices derived from either the reflection fits (Table 8) or reflection plus warm absorber fits (Table 9). The mean value of $\Gamma_{int} = 1.95$ is significantly higher than that determined from simple power-law fits to previous spectral data from *EXOSAT* and *HEAO-1*. This has a significant impact on models of the X-ray generation mechanism.

11 DISCUSSION

11.1 Observational results

The spectral fits in this work have shown results compatible with the lower sensitivity *HEAO-1* and *EXOSAT* spectral surveys, but the large area of the LAC instrument has enabled significant spectral features to be resolved. In the 2–10 keV range, the mean power-law index is found to be compatible with previous satellite observations, but with a significant spread of values. The spectrum flattens above 10 keV, indicating an additional spectral component. One possible confusing factor in these fits is the effect of a deep iron edge at an energy higher that 7.1 keV, as expected from the warm absorber, which could flatten the 10–18 keV fits. In addition, the presence of an edge will tend to *steepen* the 2–18 keV slope in a simple fit, although this is extremely unlikely to be the *sole* source of the observed spectral flattening above 10 keV. We estimate that an edge with optical depth $\tau = 0.1$ at 8 keV flattens the apparent slope in the 10–18 keV fits by $\delta\Gamma < 0.09$ and steepens the slope in the 2–18 keV fits by ~ 0.02, which is insufficient to account for the observed difference of ~ 0.3 in the slopes. Also, both the iron line and the warm absorption at soft X-ray energies will tend to *flatten* the apparent slope in the 2–18 keV fits, increasing the difference between these and the fits in the higher energy band. This evidence, together with the fact that the reflected continuum component fits are statistically required in so many cases, shows that the hard tail is best explained by reflection from cold, optically thick matter.

An emission feature, identified with iron Kα, is detected in the vast majority of sources. The energy of the line implies a fluorescent origin, in cold material. The equivalent width is large, and a hint of broadening may be present. The most plausible explanation for the iron line is that it arises in optically thick material subtending a large solid angle at the X-ray source. Whilst the precise geometry remains unclear, the most likely possibility is an accretion disc (e.g. Fabian *et al.* 1989; GF; Matt et al. 1991) or a system of optically thick clouds (Guilbert & Rees 1988; Bond & Matsuoka 1993; Sivron & Tsuruta 1993; Nandra & George 1994). Either can qualitatively reproduce the observed iron line and hard tail, but the mean parameters determined in this study suggest the former to be more likely.

A potential inconsistency arising from our *Ginga* analysis comes from a comparison with the *Einstein Observatory* SSS + MPC fits of Turner et al. (1991). These workers found little evidence for Compton reflection in their (lower energy) spectra of Seyfert galaxies, best illustrated by the example of IC 4329a. Note that this source is one of the better candidates in our sample for a reflection component, having compelling evidence for both a line and a reflection hump from *Ginga* and *Tenma* data (Miyoshi et al. 1988; Piro et al. 1990). This apparent contradiction can be explained by the warm absorber. IC 4329a shows significant absorption in the power-law plus reflection fit of Table 8, and gives a substantial improvement in χ^2 if this column is allowed to be ionized. This component is not included in the *Einstein Observatory* MPC + SSS fit. If it were, the fit would have allowed for a steeper intrinsic power law, and thereby a reflection component. A refit of the MPC + SSS data suggests that this is indeed the case (T. J. Turner, private communication).

11.2 Comparison with accretion disc models

If an accretion disc is indeed responsible for the iron line and hard tail observed in these spectra, the observed features can be used as a diagnostic of the physical conditions in the accretion flow. For instance, as the X-ray source is expected to lie very close to the central black hole, the bulk of the iron line will be produced in an environment in which extreme Doppler and gravitational shifts apply. The consequences of this are that characteristic line profiles are expected from accretion discs, dependent on the geometry and inclination (e.g. Fabian et al. 1989). Although we have not attempted to fit such profiles explicitly to the data, because of the limited resolution of the LAC detector, we now go on to discuss how the general properties of the sample relate to those expected from an accretion disc. Matt et al. (1992) have presented calculations of the expected line equivalent width, centroid energy and 1σ width for an accretion disc orbiting a Schwarzschild black hole. The main parameters that affect these quantities are the inclination and geometry of the accretion disc and the geometry of the X-ray source relative to the disc. The range of parameters considered by Matt et al. (1992) includes inner disc radius $r_i = 6$–10 (all distances measured in units of $R_g = GM/c^2$), outer radius $r_o = 10^2$–10^4, and the height of the X-ray source above the disc $h = 10$–50. Excluding the values for $r_o = 10^2$, which generally have rather small equivalent width, these workers found *mean* values for the equivalent width in the range 70–110 eV, assuming that the disc is viewed at all inclinations (we have reduced the actual values given by Matt et al. by 10 per cent to account for the fact that they used an input spectral index of $\Gamma = 1.7$ rather than the more appropriate $\Gamma = 1.9$). This agrees well with our mean value of 110 eV from the reflection fits. Again, excluding the $r_o = 10^2$ case, the mean line centroid energy should lie in the range 6.35–6.38 keV, which agrees extremely well with our observed line-energy. The range of widths is 0.4–0.8 keV, again in excellent agreement with the (limited) constraints available with the LAC. In short, the observed iron-line properties are in remarkable agreement with the prediction of the accretion disc reflection models, not only in individual cases, but for the sample as a whole.

The mean reflected continuum for the sample also agrees extremely well with that expected from the accretion disc reflection model. It can be shown that, as a function of inclination, R is roughly proportional to $W_{K\alpha}$ (Matt et al. 1992). If this is the case, we expect a mean value of $R = 0.65$–0.75, assuming solar abundances, compared to the sample mean of 0.52 ± 0.18. This, together with the fact that the individual spectra are improved so dramatically with the addition of the line and reflected continuum components, provides strong evidence that an accretion disc subtending $\sim 2\pi$ sr exists in these Seyfert galaxies, and is responsible for the production of the iron line and hard tail.

Recently, revised accretion disc reflection models have been suggested, in which the disc is partially ionized (Matt, Fabian & Ross 1993; Ross & Fabian 1993). This is expected if the disc is radiating close to the Eddington luminosity and illuminated by an intense, hard X-ray source. In this case, the line and continuum properties are somewhat different from those expected from a cold disc. In certain regimes, much larger equivalent widths can be attained, because in the hydrogen- and helium-like states the effective fluorescence yield for iron is much higher. In addition, reduced opacity at 6–7 keV means that more line photons can escape. However, in some ionization states the line can become trapped by resonant absorption, resulting in a *decrease* in the observed equivalent width. The mean energies should also be higher in the case of an ionized disc. Additionally, the reflection component may be less pronounced, as there is not as much absorption at soft X-ray energies.

Certain workers have pointed out a potential problem with the standard cold reflection model, in that there are some sources that have very large iron emission lines, sometimes *without a significant reflection hump*. For example, NGC 6814 (Turner et al. 1992), MCG-5-23-16 (Piro, Matsuoka & Yamauchi 1992), Mrk 841 (George et al. 1993), NGC 3516 (Kolman et al. 1993) and NGC 2992 from our sample all have iron-line equivalent widths significantly in excess of 150 eV, based on the simple power-law plus Gaussian fits. These sources would appear to be natural candidates for an ionized accretion disc model. Nevertheless, examining each in detail, we find that simplistic interpretations of these spectra can often be misleading. For the case of NGC 6814, it is now known that there is a periodic Galactic source in the field of view, which is likely to produce the bulk of the observed iron Kα line (Madejski et al. 1993). For MCG-5-23-16, the spectrum is complicated by the presence of a line-of-sight warm absorber. When this is included in the model, we find that not only is the line equivalent width entirely compatible with the ~ 150 eV expected from a cold, face-on accretion disc, but a significant reflection component is also allowed. NGC 3516 is similar, in that the mean equivalent width *after accounting for reflection* is only ~ 110 eV. Mrk 841 and NGC 2992 cannot be explained in this way as they still show large line strengths in the complex models. We can explain the larger equivalent widths in these sources by variability. If, as is expected in the accretion disc reprocessing scenario, the line comes from a more extended region than the primary X-rays, there may be time delays between variations in the primary continuum and reflected component. If the source is observed shortly after a significant reduction in the continuum, we might expect to observe an enhanced reflected component, which has not had time to respond to the change in X-ray flux. Repeated observations of these sources with future instrumentation will confirm or reject this. Further evidence against the widespread importance of ionized discs comes from the mean iron line energy, which strongly implies a fluorescent origin in near-neutral material, rather than a recombination line [although, if the latter were substantially gravitationally redshifted, the apparent energy could be brought back close to the 6.4 keV expected for cold iron (Matt et al. 1993)]. In summary, we find little evidence that the X-ray reprocessor is significantly ionized *in general*, but these models may be appropriate for a few sources, particularly those that apparently exhibit a warm line (e.g., NGC 7213 and Fairall-9, Pounds et al. 1994).

The applicability of a standard accretion disc model also suggests that these sources are not strongly beamed, since if the X-rays were produced in a jet perpendicular to the accretion disc, as has been suggested in many unification schemes, we would expect the reflection component and iron line to be reduced compared to the standard reflection model by relativistic beaming. Doppler enhancement of the directly

viewed continuum would result in the features being swamped, which may explain the fact that they are not seen in BL Lac type objects.

11.3 The importance of reprocessing in AGN

One important consequence of the discovery of the reflection component in AGN is the fact that a substantial amount of the emitted X-rays is absorbed in the optically thick matter which produces the line and hard tail. This must be re-emitted at the blackbody temperature of the material. Thus substantial X-ray flux must be reprocessed by this gas, and re-emitted in the optical/UV region, where the blue bump is observed. Further evidence for this reprocessing hypothesis comes from optical/UV/X-ray monitoring of NGC 5548, one of the sources in our sample. The fluxes at all wavelengths were found to be well correlated over a time-scale of weeks (Clavel et al. 1991, 1992). These variations can only be reconciled with standard accretion disc models if the UV and optical continuum radiation is reprocessed by the disc, as the observed variability time-scale is much shorter than that expected for viscous processes in the disc.

Energetically, this process is plausible. We can see from Fig. 1(b) that in the cold reflection model of GF the majority of photons between 2 and 15 keV are absorbed in the slab. Indeed, if the reprocessing material is completely neutral, then all ionizing photons down to ~ 13.6 eV are in principle available for reprocessing. However, although we have stated above that there is little evidence for *substantial* ionization of the reprocessing material in AGN, given the large continuum flux impinging on it, it seems unlikely that this material would remain completely neutral. Some photoionization models have shown that the disc is likely to become ionized (and therefore reflective) below the K-edges of carbon and/or oxygen (Brandt et al. 1993). This will reduce the reprocessed luminosity somewhat. There could also be substantial heating from harder X-rays ($E > 100$ keV) Compton-scattered in the disc, which could substantially increase the reprocessed flux. We have made a rough estimate of the likely reprocessed luminosity on average for our sources. Assuming a photon index $\Gamma = 1.95$, $R = 0.5$ and a cut-off at ~ 1 MeV, we find a reprocessed luminosity $1\text{–}4 \times L_x$ (2–10 kev) for an accretion disc geometry, depending on the ionization state of the disc. Whilst this is clearly a substantial effect, whether reprocessing *alone* can account for the blue bump in AGN remains unclear. In particular, individual cases must be examined in detail, bearing in mind that alternative geometries can produce rather different results (e.g. Nandra & George 1994).

11.4 The warm absorber

An additional bonus of our spectral study has been the detection of the warm absorber in a large number of Seyferts. The evidence for this gas component is now extremely strong. The preliminary evidence from the soft X-ray variability (e.g. Halpern 1984) has been strengthened with the discovery that ~ 50 per cent of the sample show evidence for a significant soft X-ray turnover at ~ 2 keV in the *Ginga* data. This cannot be due to a uniformly covering column of cold gas, as the *EXOSAT* LE sample showed a substantial soft X-ray flux in most cases, with little evidence for significant cold columns above the Galactic value (Turner & Pounds 1989). Added to this are the detections of iron K-absorption at 8–9 keV in many sources, and the significant improvement found when fitting a photoionized absorption profile to the sources, rather than a simple neutral column. All this evidence suggests that the absorbing column is often highly ionized. In fact, the most striking confirming evidence for the reality of the warm absorber in our *Ginga* sample comes from the *ROSAT* PSPC. The PSPC spectra of MCG-6-30-15 (Nandra & Pounds 1992), NGC 5548 (Nandra et al. 1993), NGC 3783 (Turner et al. 1993) and NGC 3227 (George et al., in preparation) all show firm evidence for absorption at oxygen-K, with implied ionization states and column densities remarkably close to those found from this work. In addition, *Ginga*/*ROSAT* simultaneous observations of NGC 4051 (Pounds et al. 1994) have shown compelling evidence for ionized material in the line of sight. All the sources mentioned above show strong evidence for a warm absorber in the *Ginga* observations.

Turner et al. (1993) have discussed the likely physical conditions in the warm absorber. Assuming a shell-like geometry and the mean parameters derived from our fits, we find a maximum radius for the warm absorber (following Turner et al. 1993) of $r_{\rm max} = 1.5 \times 10^{18} Q_{53}$, where Q_{53} is the ionizing photon flux in units of 10^{53} photon s^{-1}. Thus for our lowest luminosity warm absorber source, NGC 4051, we find $r_{\rm max} \sim 10^{17}$ cm, and for the highest, MCG-2-58-22, we obtain $r_{\rm max} \sim 10^{20}$ cm. The warm absorber must therefore be at a similar radius to, or within, the optical broad-line region. The fact that the warm absorber has a much higher ionization parameter than the broad-line clouds suggests that it must be either closer to the ionizing radiation source, or less dense than the broad-line clouds. Variability observations can give us additional constraints on the density and therefore the geometry of the warm gas, via the recombination and/or photoionization time-scales. Turner et al. (1993) also suggest that the intense X-ray flux incident on the warm absorber might result in a radiation-pressure-driven wind, apparently with a very high kinetic power. We might also identify the warm absorber with a scattering medium such as that expected in Seyfert 2 galaxies (Krolik & Kallman 1987).

It has been suggested by Ferland, Korista & Peterson (1990) that the warm absorber might constitute a 'very broad line region' (VBLR) in AGN, based on variability observations of Mrk 590. These authors suggest that the material which produces the broad wings on the Hα lines may be associated with the warm absorber. One conclusion based on these assumptions is that the warm absorber reprocesses substantial amounts of the X-ray continuum in these sources, and may even account for the whole of the blue-bump radiation. Whilst a full discussion of this point is beyond the scope of this paper, we note that the optically thick component seems a more likely source of the blue bump, based purely on energetic arguments.

The fact that large numbers of the sources in our sample show evidence for ionized material in the line of sight suggests that the covering factor of the warm absorber is high, of order 50 per cent. Indeed, it may be even higher than this, as sources with warm columns $\lesssim 10^{22}$ cm^{-2} or ionization parameters $U \gtrsim 10$ would not be detectable with *Ginga*. This estimate of the covering fraction must be reconciled with the fact that the iron-line energy in these sources is consistent

with fluorescence in near-neutral material. For the typical ionization parameter, $U \sim 1$, we expect a mean ionization state for iron greater than Fe xx and an iron-line energy 6.5–6.7 keV. Taking a column density $N_H \sim 10^{23}$ we would expect an iron-line equivalent width of order ~70–80 eV from this highly ionized material, if covering a solid angle of 4π sr at the X-ray source. Clearly, the warm absorber cannot have such a high covering fraction, as this would conflict with our observed line-energy, in such excellent agreement with the predictions of the disc reflection model. A contribution of order 20 eV would be unnoticed in our fits, given the resolution of the LAC detector, which would imply a covering factor ~25 per cent. Future spectroscopy of medium-to-high resolution will provide limits on and measurements of emission lines from the warm absorber, but we estimate from the above arguments that the ionized gas subtends ~$1-2\pi$ sr at the X-ray source.

11.5 The X-ray continuum

We find the underlying X-ray continuum in Seyfert galaxies to be rather steeper than previously thought. The value of $\Gamma = 1.7$ derived from the *EXOSAT* and *HEAO-1* fits failed to account for the effects of reflection and the warm absorber, and therefore represents an underestimate of the true intrinsic continuum slope. We find a value, using our revised 'standard' model, of $\Gamma = 1.95 \pm 0.05$ with a significant intrinsic dispersion of $\sigma_p = 0.15$. We note that a reflection spectrum with $R \sim 0.5$ produces a spectral flattening of only $\Delta\Gamma \sim 0.1$ when folded through the *Ginga* response and fitted with a power law. Therefore the existence of this flat component alone cannot explain the discrepancy between our mean intrinsic slope and the simple power-law slopes measured by *HEAO-1* and *EXOSAT*. A combination of the flattening introduced by the reflection component and that from the warm absorber seems most likely. With the low signal-to-noise ratio of these previous fits, the complex absorption at soft X-ray energies would not have been detectable. This revised value for the underlying continuum has important implications for modelling of the X-ray generation processes in AGN. Most commonly, the origin of the X-rays has been discussed in the context of a model in which soft photons are up-scattered by hot, probably relativistic electrons and pairs with a non-thermal distribution (e.g. Svensson 1987), but these models have some difficulty explaining the 'canonical' slope of $\Gamma = 1.7$, except in an uncomfortably restricted region of parameter space. $\Gamma = 2.0$ is much easier to reconcile with these models, as saturated pair-production produces this value for a wide range of the relevant parameters (e.g., hard and soft compactness, and the maximum Lorentz factor). Thus the non-thermal models were to some extent revived by the discovery of the reflection component (Zdziarski et al. 1990). A potentially more serious problem for these non-thermal models arises when attempting to describe the *hard* X-ray (50–500 keV) continua in these objects. Observations with the OSSE instrument aboard the *Compton Gamma-ray Observatory* (*GRO*) have suggested a sharp cut-off in the spectrum of NGC 4151, with an e-folding energy $E_c \sim 50$ eV (Maisack et al. 1993). Although not established for all objects, such a spectral form in more suggestive of a *thermal* electron distribution, which naturally accounts for the hard X-ray break. When generating such models, however, it is important to account for the medium-energy (2–20 keV) continua observed here with *Ginga*. Any model that fails to reproduce the revised intrinsic slope of $\Gamma \sim 2.0$ for a wide range of parameters can be immediately discounted.

11.6 Unification models

Our sample is necessarily inhomogeneous, and it is therefore difficult to reach any firm conclusions regarding the significance of our results in relation to AGN unification models. None the less, we have shown that the X-ray emission is likely to be relatively isotropic, which is consistent with the fact that most of our sources are not radio-loud. The relationship between the X-ray spectral features and radio properties is currently unclear, although it seems plausible that the iron line and hard tail are suppressed in bright, core-dominated radio sources, which are strongly beamed. Comparison of the X-ray properties with radio power or bolometric luminosity requires high-quality data for luminous quasars, which is currently scarce. In particular, the claim of an 'X-ray Baldwin effect', where the iron Kα line equivalent width is inversely proportional to the luminosity (Iwasawa & Taniguchi 1993), seems premature. We find no evidence for such an effect in our sample. Unification models of Seyfert 1 and 2 galaxies predict the existence of a molecular torus with high column density, present in all AGN. The torus serves to block the lines of sight to the nuclei in Seyfert 2 galaxies, which are hypothesized to contain identical nuclei to those in Seyfert 1s (Lawrence & Elvis 1982; Antonucci & Miller 1985). If this hypothesis is correct, we expect all Seyfert 1 galaxies to be observed approximately along the axis of symmetry of the torus. The accretion disc in these objects should therefore be close to face-on. Additionally, if the torus is optically thick, we might expect reflection and a contribution to both the emission line and the hard tail from the torus. The mean values from our sample suggest that this is *not* the case, so we must conclude that, in Seyfert 1 galaxies, the torus either is absent, or is of low optical depth ($\tau_T < 1$). This raises interesting questions for the unification models.

12 CONCLUSIONS

In Table 10, we show a summary of the properties of the individual Seyfert galaxies, together with the mean values of the important parameters for each source. Intrinsic spectral indices have been taken from power-law plus reflection fits or power-law, reflection plus warm absorber fits where appropriate. The line-energies are from the power-law plus line fits, and the equivalent widths from fits including the reflection component. As a final illustration of the importance of the phenomena described above, we show, in Fig. 1(b), the composite spectrum (see Section 4) for all our observations added together, fitted with our revised standard model of a power law, warm absorber, line and reflection hump. All features are required at high statistical significance and the mean spectrum gives very similar parameters to those derived from the individual fits described in this paper. We have not added any systematic error to account for uncertainties in background-subtraction or poor calibration

Table 10. Summary of the properties of individual AGN.

Name	Line	N_H	Edge	Warm	Refl.	Γ_{int}	$E_{K\alpha}$	$W_{K\alpha}$	$\log N_H$*	R
Mrk 335	√	√	√	√	√	2·39 ± 0·15	6·02 ± 0·52	40 ± 120	23·3 ± 0·7	22·4 ± 31·0
NGC 526A	√	√				1·49 ± 0·21	6·75 ± 0·58	220 ± 170	–	0·8 ± 16·7
Fairall-9	√					1·94 ± 0·09	6·86 ± 0·31	120 ± 70	–	0·0 ± 1·3
3C 111	√	√				1·77 ± 0·06	7·37 ± 1·02	30 ± 60	–	0·0 ± 0·4
Akn 120					√	1·93 ± 0·11	–	–	–	4·8 ± 19·2
NGC 2110	√	√		√		1·93 ± 0·11	6·49 ± 0·25	160 ± 60	22·6 ± 0·3	0·0 ± 1·2
NGC 2992	√	√		√		2·30 ± 0·21	6·43 ± 0·16	440 ± 100	22·8 ± 0·4	1·1 ± 24·2
NGC 3227	√	√			√	1·95 ± 0·07	6·43 ± 0·15	150 ± 30	22·4 ± 0·4	1·2 ± 1·7
MCG-5-23-16	√	√	√	√		1·86 ± 0·12	6·56 ± 0·20	260 ± 70	22·9 ± 0·2	0·0 ± 1·5
NGC 3516	√	√			√	2·08 ± 0·09	6·29 ± 0·15	110 ± 90	–	16·5 ± 14·2
NGC 3783	√	√		√		2·11 ± 0·07	6·22 ± 0·14	180 ± 40	22·96 ± 0·08	0·0 ± 0·5
NGC 4051	√	√	√	√	√	1·84 ± 0·09	5·92 ± 0·38	60 ± 60	22·8 ± 0·5	7·3 ± 13·8
NGC 4593	√				√	1·81 ± 0·07	6·55 ± 0·31	90 ± 60	–	2·1 ± 3·9
MCG-6-30-15	√	√	√	√	√	2·12 ± 0·04	6·21 ± 0·10	140 ± 20	22·83 ± 0·06	0·8 ± 0·7
IC 4329A	√	√		√	√	2·03 ± 0·04	6·37 ± 0·12	110 ± 20	22·0 ± 0·3	0·8 ± 0·6
NGC 5506	√	√			√	2·08 ± 0·05	6·39 ± 0·13	130 ± 30	–	2·7 ± 2·1
NGC 5548	√	√	√	√	√	1·81 ± 0·02	6·35 ± 0·11	113 ± 18	22·66 ± 0·18	0·7 ± 0·4
Mrk 841	√	√				2·30 ± 0·02	6·28 ± 0·29	210 ± 270	–	31·8 ± 95·7
3C 382	√	√		√	√	1·73 ± 0·11	6·50 ± 0·25	250 ± 90	22·9 ± 2·0	0·2 ± 3·6
3C 390.3					√	1·86 ± 0·03	–	–	–	1·2 ± 0·5
Mrk 509	√				√	1·86 ± 0·02	6·55 ± 0·24	60 ± 30	–	2·0 ± 0·9
H2106-099	√				√	1·96 ± 0·11	6·56 ± 1·74	40 ± 120	–	2·3 ± 8·9
NGC 7172	√	√			√	1·87 ± 0·05	6·44 ± 0·47	40 ± 40	–	1·2 ± 1·4
NGC 7213	√	√		√		1·96 ± 0·08	6·72 ± 0·20	130 ± 40	22·8 ± 0·3	0·0 ± 0·5
NGC 7314	√	√			√	1·91 ± 0·11	6·03 ± 0·66	100 ± 90	–	2·0 ± 52·3
NGC 7469	√				√	1·97 ± 0·05	6·47 ± 0·54	70 ± 70	–	3·8 ± 6·7
MCG-2-58-22	√	√	√	√		1·67 ± 0·08	6·46 ± 0·28	150 ± 50	23·0 ± 0·3	0·1 ± 1·1

around the instrumental silver line at 20–25 keV, so, whereas the composite fit is formally unacceptable, the improvement relative to the power law and the overall goodness of fit are remarkable.

In summary, our conclusions are as follows.

(1) Power-law fits give an unacceptable fit to the 2–20 keV X-ray spectra of Seyfert galaxies, with the excess χ^2 arising because of both line and continuum spectral features.

(2) Notwithstanding these complexities, the apparent continuum slopes in the 2–18 keV (2–10 keV) range derived from these fits are compatible with those found previously by *HEAO-1* and *EXOSAT* ($\Gamma = 1.73 \pm 0.05$), with a significant spread ($\mu_p = 0.15$).

(3) By contrast, when fits are conducted above 10 keV, the continuum is found to be considerably flatter than in the broader (effectively lower) energy range. Here we find $\Gamma = 1.46 \pm 0.08$, again with a significant intrinsic spread of $\sigma_p = 0.22$.

(4) Soft X-ray absorption is found to be common, with ~50 per cent of objects showing $N_H > 10^{21}$ cm^{-2}. This excess over the Galactic column density, greater than that indicated by the strong X-ray fluxes observed by *EXOSAT* and *ROSAT*, strongly suggests that the absorption is complex, and likely to be due to ionized gas.

(5) Iron-line emission is a very common property of low-luminosity Seyferts, with all but two of our 27 sample objects showing evidence for a line. The mean line-energy is 6.37 ± 0.07 keV, consistent with fluorescent emission from cold iron. The mean equivalent width is 140 ± 20 eV, in power-law plus line fits, but a more plausible continuum model, which includes a reflection component, gives $W_{K\alpha} = 114 \pm 18$.

(6) Iron K-shell absorption edges are another common observed feature, detected in at least 12 of the sources. Equivalent hydrogen column densities are typically ~10^{23} cm^{-2} at an energy ~8 keV. These also indicate a substantial column of strongly photoionized gas in the line of sight to Seyfert galaxies.

(7) The strength of the iron emission feature cannot be explained by cold line-of-sight gas, even if it has a substantially enriched metal abundance, due to the lack of a strong ($N_H > 10^{23}$ cm^{-2}), soft X-ray cut-off in most sources. The highly ionized gas may contribute to the emission at some level but is not, in general, the major source of the iron line. The most plausible explanation for the Kα line is fluorescence in optically thick material subtending a large solid angle at the continuum source. We find this to be a good model for the observed feature if the material subtends ~2π sr at the X-ray source.

(8) Compton down-scattering and absorption in the same optically thick gas result in a reflected continuum which acompanies the iron line. This is a natural explanation for the hard tail observed in the data and fits the spectra well, producing a significant statistical improvement in most sources. The ratio of the mean strength of the reflected component to the iron-line equivalent width indicates an iron abundance close to the cosmic value. The strengths of the line and hard tail show that a flattened geometry (probably an accretion disc) is the most likely source of these features.

(9) We have modelled the warm absorber using a photoionization code, and find that not only does this explain the presence of the absorption feature at iron-K, but also for many sources it provides a better fit to the opacity profile at low energies, compared to that expected for cold gas. About 50 per cent of our sources show evidence for highly ionized gas in the line of sight.

(10) When the effects of reflection and the warm absorber have been accounted for, we find the underlying mean X-ray continuum slope to be $\Gamma = 1.95$, with a small, but

significant, intrinsic dispersion. This result is relevant to models of the generation of X-rays in AGN.

It is clear that the *Ginga* X-ray spectra have wide-reaching implications for the understanding of AGN. Further advancement in our knowledge of these objects will be brought about with the next generation of X-ray detectors, beginning with *ASCA*, which will be able to study the line and warm absorber properties of these sources in greater detail.

ACKNOWLEDGMENTS

The work described here would not have been possible without the assistance of many colleagues. We gratefully acknowledge the members of the *Ginga* team for building and operating the satellite so successfully. Much of the analysis described here was carried out using software written by members of the Leicester University X-ray Astronomy Group, and particular thanks go to Rees Williams and Jackie Butcher for their efforts in perfecting the analysis system and background-subtraction. We also thank Ian George and Andy Fabian for use of their Monte Carlo models and many discussions, Tahir Yaqoob for use of his warm absorber model, Giorgio Matt for discussions regarding the disc reflection models, and Chris Done for a critical reading of the manuscript. KN acknowledges receipt of a Research Associateship awarded by the SERC.

REFERENCES

Antonucci R. R., Miller J. S., 1985, ApJ, 297, 621
Awaki H., 1991, PhD thesis, Univ. Nagoya
Bevington P. R., 1969, Data Reduction and Error Analysis for the Physical Sciences. McGraw-Hill, New York
Bond I. A., Matsuoka M., 1993, MNRAS, 265, 619
Brandt W. N., Fabian A. C., Nandra K., Tsuruta S., 1993, MNRAS, 265, 996
Clavel J. et al., 1991, ApJ, 366, 64
Clavel J. et al., 1992, ApJ, 393, 113
Fabian A. C., Rees M. J., Stella L., White N. E., 1989, MNRAS, 238, 729
Ferland G., Korista K. T., Peterson B. M., 1990, ApJ, 363, L1
Fiore F., Elvis M., Mathur S., Wilkes B., McDowell J. C., 1993, ApJ, 415, 129
George I. M., Fabian A. C., 1991, MNRAS, 249, 352 (GF)
George I. M., Nandra K., Fabian A. C., Done C., Day C. S. R., 1993, MNRAS, 260, 111
Guilbert P. W., Rees M. J., 1988, MNRAS, 233, 475
Halpern J. P., 1984, ApJ, 281, 90
Hayashida K. et al., 1989, PASJ, 41, 373
Holt S. S., Mushotzky R. F., Becker R. H., Boldt E. A., Serlemitsos P. J., Szymkowiak A. E., White N. E., 1980, ApJ, 241, L13
Iwasawa K., Taniguchi Y., 1993, ApJ, 413, L15
Kolman M., Halpern J. P., Martin C., Awaki H., Koyama K., 1993, ApJ, 403, 592
Krolik J. H., Kallman T. R., 1987, ApJ, 329, L5
Lampton M., Margon B., Bowyer S., 1976, ApJ, 208, 177
Lawrence A., Elvis M., 1982, ApJ, 256, 410
Lightman A. P., White T. R., 1988, ApJ, 335, 57
Maccacaro T. et al., 1988, ApJ, 326, 680
Madejski G. M. et al., 1993, Nat, 365, 626
Maisack M. et al., 1993, ApJ, 407, L61
Makino F. and The *ASTRO-C* Team, 1987, Astron. Lett. Commun., 25, 223
Makishima K., 1986, in Mason K. O., Watson M. G., White N. E., eds, The Physics of Accretion onto Compact Objects. Springer-Verlag, Berlin, p. 249
Malkan M. A., Sargent W. L., 1982, ApJ, 254, 22
Matsuoka M., Yamauchi M., Piro L., Murakami R., 1990, ApJ, 361, 440
Matt G., Perola G. C., Piro L., 1991, A&A, 245, 75
Matt G., Perola G. C., Piro L., Stella L., 1992, A&A, 257, 63
Matt G., Fabian A. C., Ross R. R., 1993, MNRAS, 262, 179
Matthews W. G., Ferland G. J., 1987, ApJ, 323, 456
Miyoshi S. et al., 1988, PASJ, 40, 127
Morrison R., McCammon D., 1983, ApJ, 270, 119
Mushotzky R. F., 1984, Adv. Space Res., 3, 10
Nandra K., 1991, PhD thesis, Univ. Leicester
Nandra K., George I. M., 1994, MNRAS, 267, 974
Nandra K., Pounds K. A., 1992, Nat, 359, 215
Nandra K., Pounds K. A., Stewart G. C., Fabian A. C., Rees M. J., 1989, MNRAS, 236, 39P
Nandra K., Pounds K. A., Stewart G. C., 1990, MNRAS, 242, 660
Nandra K., Pounds K. A., Stewart G. C., George I. M., Hayashida K., Makino F., Ohashi T., 1991, MNRAS, 248, 760
Nandra K. et al., 1993, MNRAS, 260, 504
Pan H.-C., Stewart G. C., Pounds K. A., 1990, MNRAS, 242, 177
Piro L., Matsuoka M., Yamauchi M., 1990, ApJ, 360, L35
Piro L., Matsuoka M., Yamauchi M., 1992, in Tanaka Y., Koyama K., eds, Frontiers in X-ray Astronomy. Univ. Acad. Press, Tokyo, p. 527
Pounds K. A., Nandra K., Stewart G. C., Leighly K., 1989, MNRAS, 240, 769
Pounds K. A., Nandra K., Stewart G. C., George I. M., Fabian A. C., 1990, Nat, 344, 132
Pounds K. A., Nandra K., Fink H. H., Makino F., 1994, MNRAS, 267, 193
Ross R. R., Fabian A. C., 1993, MNRAS, 261, 74
Shields G. A., 1978, Nat, 272, 706
Sivron R., Tsuruta S., 1993, ApJ, 402, 420
Stark A. A., Gammie C. F., Wilson R. W., Bally J., Linke R. A., Heiles C., Hurwitz M., 1992, ApJS, 78, 77
Svensson R., 1987, MNRAS, 227, 403
Turner M. J. L. et al., 1989, PASJ, 41, 345
Turner T. J., Pounds K. A., 1989, MNRAS, 240, 833
Turner T. J., Done C., Mushotzky R. F., Madejski G., Kunieda H., 1992, ApJ, 391, 102
Turner T. J., Nandra K., George I. M., Fabian A. C., Pounds K. A., 1993, ApJ, 419, 127
Turner T. J., Weaver K. A., Mushotzky R. F., Holt S. S., Madejski G. M., 1991, ApJ, 381, 85
Warwick R. S., Sembay S., Yaqoob T., Makishima K., Ohashi T., Tashiro M., Kohmura Y., 1993, MNRAS, 265, 412
Williams O. R. et al., 1992, ApJ, 389, 157
Yaqoob T., Warwick R. S., 1991, MNRAS, 248, 773
Zdziarski A. A., Ghisellini G., George I. M., Svensson R., Fabian A. C., Done C., 1990, ApJ, 363, L1